A comprehensive rocket and radar study of midlatitude spread *F*

G. D. Earle,[1] P. Bhaneja,[2] P. A. Roddy,[3] C. M. Swenson,[4] A. Barjatya,[5] R. L. Bishop,[6] T. W. Bullett,[7] G. Crowley,[8] R. Redmon,[9] K. Groves,[3] R. Cosgrove,[10] and Sharon L. Vadas[11]

Received 25 March 2010; revised 14 July 2010; accepted 9 September 2010; published 31 December 2010.

[1] An instrumented sounding rocket launched from Wallops Island Virginia has flown through a midlatitude spread *F* (MSF) event in conjunction with simultaneous ionosonde, HF radar, and 244 MHz scintillation observations from the ground. The in situ measurements include the electric field, horizontal neutral wind, and plasma density within the spread *F* region. The ground-based HF radar measurements of wave signatures in the bottomside *F* region ledge reveal the presence of waves propagating to the north and northwest prior to and during the spreading event. The periods of these bottomside waves range from 16 to 60 min, and they are shown to be associated with a strong tropical storm located ~2000 km southeast of the launch site. Enhancements in the auroral current system occur about an hour before the MSF first appears, but none of the observed waves can be attributed to this source. The new phase-sensitive ionosonde system operated at Wallops Island during the experiment confirms the long-standing hypothesis that this particular spread *F* event arises from multipath echoes distributed over a wide field of view in the bottomside *F* region. Evidence of vertically displaced plasma that could produce such multipath echoes is observed in the rocket data at and above the *F* region peak over spatial scales smaller than the wavelengths observed on the bottomside ledge by the HF radar, but similar to the range separation given by the high resolution ionosonde echoes when the scale lengths of the structures are interpreted in magnetic coordinates. No significant plasma density structures smaller than a few kilometers are observed in the rocket data, and no unusual scintillation is observed along a path coincident with the rocket trajectory.

Citation: Earle, G. D., et al. (2010), A comprehensive rocket and radar study of midlatitude spread *F*, *J. Geophys. Res.*, *115*, A12339, doi:10.1029/2010JA015503.

1. Introduction

[2] Previous analysis of midlatitude spread *F* (MSF) statistics at Wallops Island, Virginia using ground-based digisonde data have shown that it has strong seasonal and solar cycle dependences [*Bhaneja et al.*, 2009]. The study described here includes in situ data, which give a more detailed picture of an MSF event at this site. The experiment reveals for the first time the plasma density structures and the local *F* region neutral wind and electric field vectors within an active MSF event.

[3] Most theoretical treatments of midlatitude irregularities invoke gravity waves and/or traveling ionospheric disturbances (TIDs) as a probable cause [*Bowman*, 1990; *Miller*, 1997]. *Hines* [1960] established a connection between traveling ionospheric disturbances and gravity waves. A study by *Bowman* [1990], using data from two ionosondes near Brisbane, Australia, showed a strong correlation between daytime TIDs and nighttime spread *F*. Waves that perturb the ionosphere may be generated by intense convective activity associated with tropical storms and hurricanes [*Bauer*, 1958; *Rottger*, 1977; *Kelley*, 1997; *Bishop et al.*, 2006]. Since gravity waves/TIDs can be launched by convective events in the lower atmosphere [*Alexander et al.*, 1995], by body forces created by dissipating gravity waves in the thermosphere [*Vadas and Liu*, 2009], and by auroral heating at E and *F* region altitudes

[1]William B. Hanson Center for Space Sciences, University of Texas at Dallas, Richardson, Texas, USA.
[2]NGDC, CIRES, Boulder, Colorado, USA.
[3]Air Force Research Laboratory, Space Vehicles Directorate, Hanscom AFB, Massachusetts, USA.
[4]Department of Electrical and Computer Engineering, Utah State University, Logan, Utah, USA.
[5]Physical Sciences Department, Embry-Riddle Aeronautical University, Daytona Beach, Florida, USA.
[6]The Aerospace Corporation, Los Angeles, California, USA.
[7]Space Weather Observations and Applications, NDGC, CIRES, Boulder, Colorado, USA.
[8]Atmospheric and Space Technology Research Associates LLC, San Antonio, Texas, USA.
[9]NOAA, NGDC, Boulder, Colorado, USA.
[10]Center for Geospace Studies, SRI International, Menlo Park, California, USA.
[11]CoRA Division, NorthWest Research Associates, Boulder, Colorado, USA.

0148-0227/10/2010JA015503

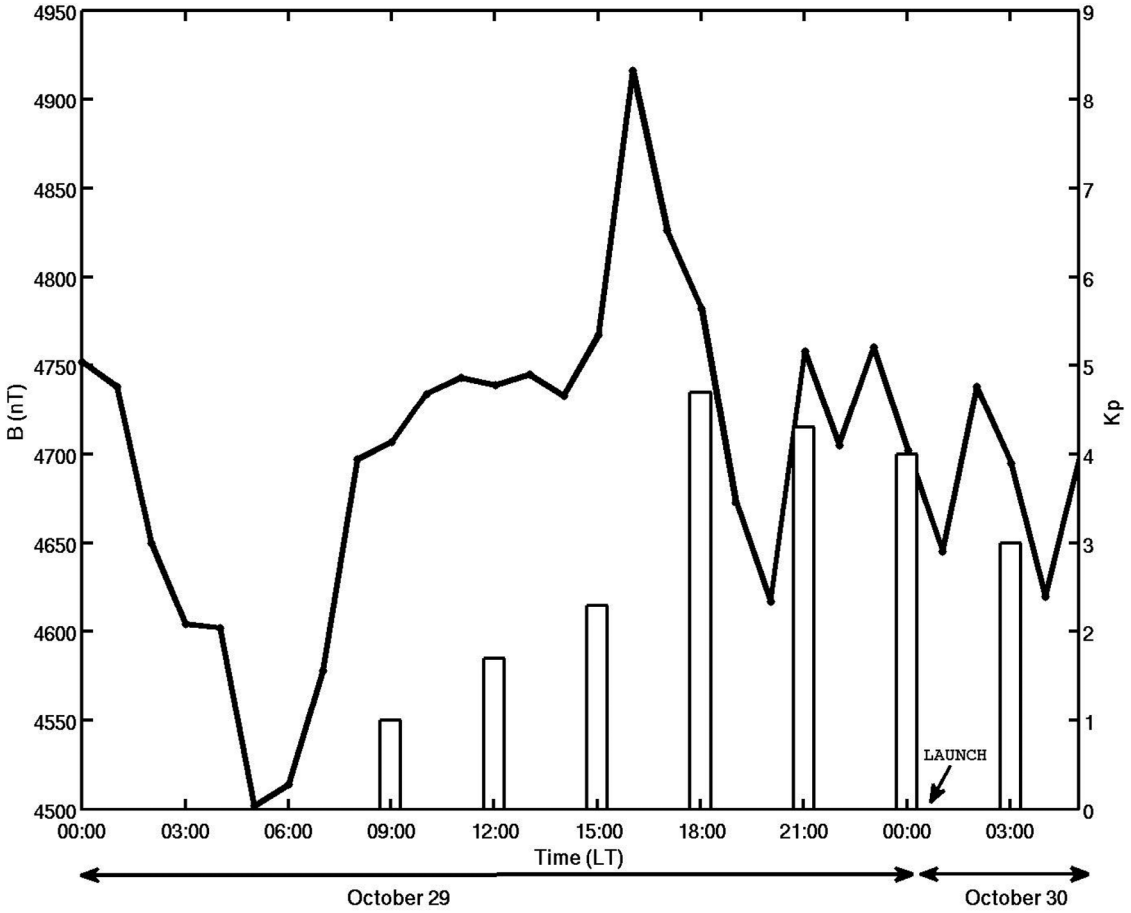

Figure 1. Kp values prior to and during the MSF event into which the rocket was launched (right axis), superimposed with magnetometer data from Fort Churchill for the period prior to the rocket launch.

[*Hocke and Schlegel*, 1996], all of these phenomena are candidate sources to perturb the midlatitude ionosphere and trigger midlatitude spread *F*.

[4] Radar studies related to MSF formation and development have been published repeatedly over the last four decades. *Mathews and Harper* [1972] reported an observation of spread *F* at Arecibo for one night in January and suggest that it may occur due to plasma density structure ionosphere caused by enhanced ionization stimulated by waves. *Behnke* [1979] used the Arecibo Observatory in an azimuth scanning mode and noted structures in the plasma that he called "height-layer bands." The bands were associated with large electric fields, which were attributed to the Perkins instability [*Perkins*, 1973]. More recent work by *Cosgrove and Tsunoda* [2002b] has suggested that the electric fields may arise from polarization of an underlying sporadic *E* layer and that the height bands may be caused by these electric fields through an *E-F* region coupling effect [*Cosgrove*, 2007].

[5] Despite a preponderance of ground-based observations from radars, ionosondes and optical imagers [e.g., *Kelley et al.*, 2000, and references therein], no previous study has gathered in situ data within a midlatitude spread *F* event while simultaneously observing *F* region spreading and gravity waves with ground-based radar. For this reason there has been no information on the colocated winds, electric fields, and plasma density structures within MSF. The collaborative rocket and radar study described here therefore provides the most comprehensive data set yet assembled for developing a systemic understanding of MSF at high midlatitudes (Wallops Island).

2. Prevailing Atmospheric Conditions

2.1. Magnetic Conditions

[6] The Kp magnetic index values were very low for several days preceding the rocket experiment, but a sudden increase in Kp was observed in the afternoon prior to the nighttime rocket launch. Figure 1 shows the overall Kp values and the Fort Churchill magnetometer data for the day prior to the launch. Kp increased from quiet levels (2+) to active (5−) about 6 h prior to the appearance of MSF at Wallops Island and remained at disturbed levels during the rocket flight. The Fort Churchill data show large excursions roughly coincident with the Kp variations, which indicate large currents near the Wallops longitude sector that could generate significant atmospheric heating, and potentially launch gravity waves that could trigger MSF over Wallops.

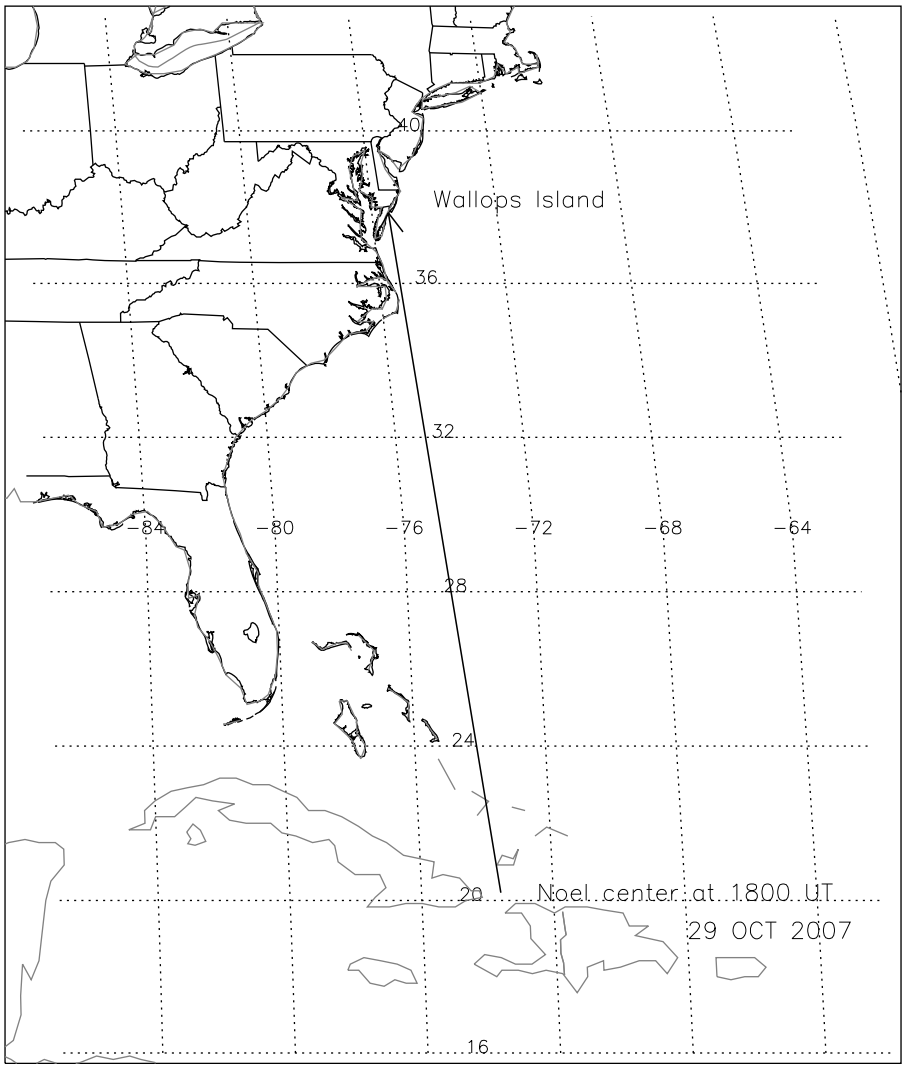

Figure 2. Map showing the location of tropical storm Noel on 29 October 2007 at 1800 UT (1400 LT), roughly 10 h prior to the onset of MSF over Wallops Island.

2.2. Weather Conditions

[7] A tropical storm that eventually evolved into hurricane Noel formed off the southeast coast of Haiti on the afternoon of 27 October [*Brown*, 2008]. Over the next several days it traveled toward the northeast through the Bahamas, causing torrential rains, floods, and consequent loss of life in the chain of islands stretching from Haiti to the Bahamas. On 29–30 October the storm center stalled over the northeast coast of Cuba. In the evening hours prior to the rocket experiment the hurricane was ~2000 km south–southeast of the Wallops Island launch site and was moving slowly westward and producing surface wind speeds of ~83 km/h. Figure 2 shows the position of the hurricane about 10 h prior to the onset of MSF over Wallops Island. The convective activity associated with this storm provides another strong source of gravity waves that could influence the ionospheric MSF conditions at the launch site.

3. Experiment Description

[8] The rocket was launched from Wallops Island, Virginia (37.95°N, 284.53°E, 67.5° dip angle) on 30 October 2007 at 12 min after local midnight or 0412 UT. It flew along an azimuth of 114° and reached apogee near 394 km. The decision to launch the rocket was based on the presence of an active, long duration MSF event over Wallops Island. The spread *F* condition into which the rocket was launched had been active for ~30–45 min prior to the launch and included both range and frequency spreading. In addition to the instrumentation aboard the rocket, a number of ground-based systems monitored the ionosphere over Wallops Island and along the flight path of the rocket. All of these systems are described below.

3.1. Ground-Based Instruments

[9] The ground-based instruments used in this experiment included the standard Wallops digisonde system for monitoring the onset and severity of spread *F*; this system was the primary prelaunch diagnostic. The digisonde is a wide-beam pulsed radar system that delivers 10 kW peak power and utilizes fast switching frequency synthesis to cover a frequency range of 500 kHz to 30 MHz [*Reinisch et al.*, 1989]. The sounder measures the parameters required to

characterize the reflected wave: amplitude, phase, and frequency, for both the ordinary (O) and extraordinary (X) components of the reflected waves [*Bibl and Reinisch*, 1978; *Rishbeth and Davis*, 2001]. For this experiment, the instrument operated in an ionogram mode where echo power was recorded at discrete frequencies as the radar stepped through a preset frequency range; in this case using a step-size of 50 kHz. The ionogram duty cycle is programmable, and to provide maximum time resolution for monitoring the onset of MSF, the time between successive ionograms was set at 5 min during the prelaunch period.

[10] In addition to the digisonde, a higher-resolution phase-sensitive dynasonde system was installed at the Wallops Geophysical Observatory in support of this mission. Like the digisonde, this radar uses a wide-beam stepped frequency transmitter. However, the dynasonde receiver is sensitive to the phase of the reflected signals and has significantly better range and frequency resolution than the digisonde system. The dynasonde data were not available in real time for use as prelaunch diagnostics, although this capability is possible for future missions.

[11] The experiment also included 244 MHz scintillation detectors at Martha's Vineyard oriented to look for scintillations along the flight path southeast of Wallops Island, and a portable Doppler radar system utilizing three transmitters, and a single receiver to monitor traveling ionsopheric disturbances (TIDs) in the bottomside ionosphere over Wallops. The latter system is called TIDDBIT; a description of its operational capabilities is given by G. Crowley and F. S. Rodrigues (Characteristics of traveling ionospheric disturbances observed by the TIDDBIT radar, submitted to *Journal of Geophysical Research*, 2010). By using two frequencies and multiple propagation paths, TIDDBIT monitored the propagation characteristics of traveling ionospheric disturbances (TIDs) on the bottomside *F* region ledge in the nighttime ionosphere prior to and during the sounding rocket investigation (G. Crowley et al., TIDDBIT HF Doppler Sounder measurements of TIDs during the Wallops Island rocket launch of October 2007, submitted to *Journal of Geophysical Research*, 2010).

[12] Aside from monitoring the mesoscale (10–100 km) and larger ionospheric fluctuations on the night of the launch, the ground-based systems also gathered data sets over several weeks prior to the flight. These data sets allow comparative analysis of ionospheric behavior on several other nights on which MSF occurred, as well as many nights on which no MSF was observed. Crowley and Rodrigues (submitted manuscript, 2010) and *Vadas and Crowley* [2010] describe these observations in detail. The focus of this paper is the observations on the night of the rocket flight, particularly the comparison between ground-based and in situ observations, and evidence of plasma density structures and high altitude gravity waves coincident with midlatitude spread *F*.

3.2. In Situ Instruments

[13] The instruments carried by the rocket include the Hanson anemometer for thermospheric investigations (HATI), a vector electric field instrument (VEFI), a fixed-bias Langmuir probe (DCP), and a plasma impedance probe (PIP). HATI and VEFI were designed and built by the University of Texas at Dallas, while DCP and PIP were provided by Utah State University. The HATI and VEFI instruments flew on the main payload, and the DCP and PIP flew on a daughter payload that was deployed at an altitude of about 100 km, simultaneously exposing the Langmuir probe.

[14] The HATI instrument measures the horizontal neutral wind subject to the assumption that the vertical wind is negligible in comparison. It consists of a hemispherical sensor head with four symmetrically located apertures, each 30° off the central axis. Each aperture opens into a separate chamber, and each chamber contains an ion gauge to measure the pressure. *Hanson et al.* [1992] show the basic HATI instrument configuration and describe the principles of operation for a satellite-based version of the instrument. The rocket instrument is similar, and the analysis principles are the same.

[15] The basic idea is that the HATI instrument measures the pressure in all four chambers simultaneously as the rocket flies through the *F* region. The pressure in each chamber depends on the angle of attack of its aperture relative to the ambient neutral gas flow. The pressure measured in each chamber is dominated by the ram effect due to the rocket's upward motion, but small modulations are also produced by variations in the motion of the ambient neutral gas. The rocket spins slowly at 0.33 revolutions per second during flight and continuously changes its orientation, so the angle of attack for each of the four apertures varies constantly, but the rates of change of these effects are much faster than the variations of the neutral atmospheric winds. Since the attitude, position, and velocity of the rocket are well known from radar tracking, onboard GPS measurements and the rocket's gyroscopic control systems, postflight analysis can determine the horizontal neutral wind direction and amplitude along the flight path.

[16] VEFI measures the electric fields perpendicular to **B** by assuming $\mathbf{E} \cdot \mathbf{B} = 0$; this is a good approximation in the midlatitude *F* region, where the parallel conductivity is much greater than the Hall and Pedersen conductivities. The standard floating double-probe technique is used, as described by *Fahleson et al.* [1970]. The VEFI instrument uses high-impedance amplifiers to measure the potential difference between titanium nitride-plated stainless steel spheres mounted on the ends of two 1.6 m booms; when divided by the boom length, this measurement gives the instantaneous electric field along the direction of the boom.

[17] The daughter payload carried a fixed-bias Langmuir probe (DCP) for high-resolution relative density measurements and a swept frequency plasma impedance probe (PIP) for absolute density measurements. The cylindrical DCP is 0.0254 m length and 0.00635 m in diameter. This small size is required to maintain a sufficiently large spacecraft to probe area ratio to enable reliable measurements. The probe has guard electrodes to mitigate fringing field effects, and its surface is heated prior to launch to remove surface contamination that might bias the measurements. If the plasma density is large enough and the signal-to-noise ratio is good, the electron neutral collision frequency and electron temperature can also be determined from the PIP measurements. The resolution of the DCP was $\sim 2.3 \times 10^4$ cm^{-3} on this experiment. Only plasma density data are presented here, since the other

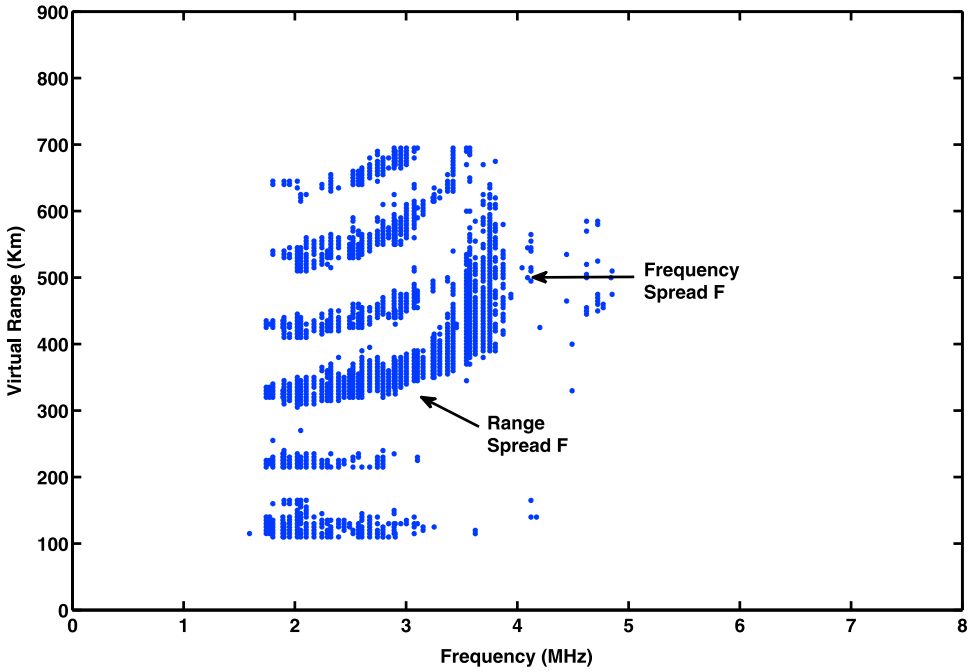

Figure 3. Ionogram showing O mode traces on 30 October at 1215 AM local time, just 3 min after the rocket launch.

parameters are less relevant to our investigation and require significantly more processing to infer from the data.

4. Data Presentation

4.1. Ground-Based Data

[18] The ground-based data obtained prior to and coincident with the rocket experiment include ionograms from the digisonde and dynasonde instruments, the TIDDBIT HF-radar, and the scintillation detectors.

4.2. Digisonde and Dynasonde Diagnostics

[19] The ionograms from the digisonde at the time of launch clearly show a spread *F* signature. Figure 3 is an ionogram obtained 3 min after the launch or about 1 min before the rocket reached the altitude of the spread *F*. The traces below the range spread *F* are caused by a sporadic *E* layer, which was intermittently blanketing prior to our MSF event. The layer either dispersed or moved out of the field of view about 45–60 min prior to the launch. The multihop echoes at *F* region heights are due to the multiple reflections of the pulse (from the ionosphere to the ground, back to the ionosphere, and back to the receiver). Both range and frequency spread *F* are visible in Figure 3.

[20] The new dynasonde system at Wallops Island is similar to the digisonde but responds to the phase rather than the amplitude of the reflected wave. This new system is inherently more sensitive and provides much better range resolution than a typical digisonde. Figure 4 shows a dynasonde image obtained during the rocket flight and provides a better resolved image of the spreading event shown in Figure 3. The ionogram in Figure 3 shows both range and frequency spread *F* as continuous overlapping echo bands, while the increased range resolution of the dynasonde shows the discrete O mode traces that comprise these spread echoes.

[21] Both Figures 3 and 4 show only the ordinary mode (O mode) traces of the ionograms. The extraordinary mode (X mode) shows similar spreading features but does not add any new information. Furthermore, detailed analysis of the X mode requires precise knowledge of the magnetic field geometry and thereby adds a significant level of complexity to the data analysis procedure. For this reason, the O mode data have historically been more widely relied upon when analyzing ionosonde data, and we follow this precedent in this paper.

[22] Figure 4 (top) shows the signal-to-noise ratio (SNR) of the backscattered echoes coincident with the rocket flight. Figure 4 (bottom) displays the ordinary mode signal-to-noise ratio as a function of virtual range; it contains numerous echo signatures that are close replicas of the impulse response of the receiver. A discrete echo at a single range produces such a receiver response, while a diffuse echo broadens this response in range. Echoes associated with the sporadic *E* layer have been identified and discarded prior to plotting, as have X mode signals that leak into the data at a low level.

[23] The spread *F* signatures observed on the normal ionograms are resolved into six distinct traces by the more sensitive dynasonde system. These six discrete echoes are identified and numbered 1–6 in Figure 4 (bottom), and the range of the peak of the impulse response is determined to the nearest 1 km. The range extent of the echoes is 58 km, which represents a volume of up to 58 km in altitude and approximately 200 km in horizontal distance. These data are thus consistent with the presence of horizontal corrugations in the *F* region of the ionosphere within the field of view of the system, each of which produces a distinct trace in the ionogram. Reflection from smaller scale irregularities is not evident in these observations.

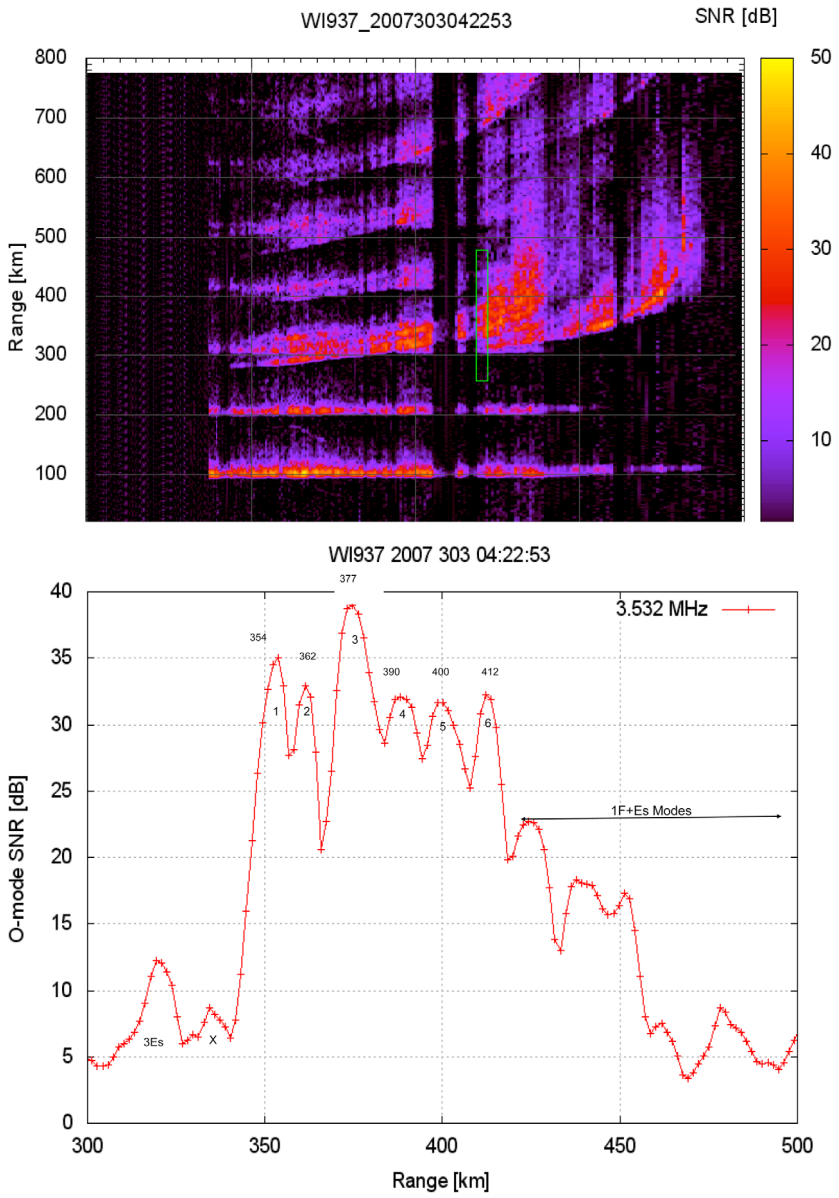

Figure 4. (top) An ionogram generated from the dynasonde system at Wallops Island during the rocket flight. (bottom) O mode signal-to-noise ratio versus virtual height at 3.5 MHz. Note that the spreading is resolved into six discrete overlapping echo traces by the dynasonde.

4.3. TID Activity Coincident With the MSF Event

[24] The HF Doppler technique is a sensitive method for detecting transient changes in the ionosphere and was used in the 1960s to 1980s to study TIDs [*Georges*, 1968]. The Doppler system is a relatively low-cost instrument, and because HF Doppler systems have low power consumption, temporal resolution can be maintained for many days at a relatively low cost. For example, the Antarctic HF Doppler system operated continuously for 5 years [*Crowley*, 1985; *Crowley et al.*, 1987], and a system operated continuously in the UK for several months [*Crowley and McCrea*, 1988]. The basic technique is to measure changes in the propagation path of HF waves reflected from the bottomside of the *F* region ionosphere. As a TID propagates through the ionosphere, it produces corrugations in the isoionic contours, so that an HF signal at a fixed frequency is reflected from a constantly changing height as the TID passes by. The change in phase-path is measured as a tiny Doppler shift in the received frequency of the HF wave. Correlation of these small Doppler shifts permits information to be gleaned about the TIDs. Cross-spectral analysis of the signals obtained from three different propagation paths yields information on individual waves as they pass over the sounder array [*Crowley*, 1985; Crowley and Rodrigues, submitted manuscript, 2010; Crowley et al., submitted manuscript, 2010]. The TIDDBIT radar deployed for this rocket launch (Crowley et al., submitted manuscript, 2010) obtains the horizontal and vertical wavelengths and phase-trace speeds as a function of wave period, for waves with periods ranging from ~1 to 90 min. *Vadas and Crowley* [2010] study in detail the waves observed during this experiment with periods greater than 15 min.

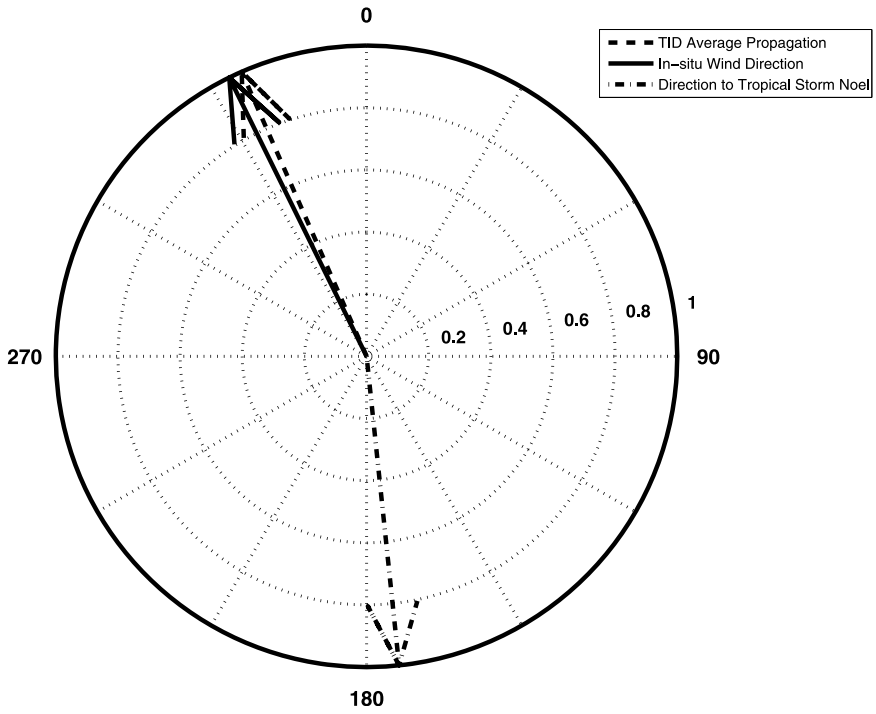

Figure 5. Plot showing unit vectors indicating the average direction the waves observed by the TIDDBIT system, the direction of the *F* region wind within the MSF event (see section 5.2), and the direction vector from Wallops Island to tropical storm Noel. Zero corresponds to geographic north.

[25] The sounder measured a large number of waves during the launch period (Crowley et al., submitted manuscript, 2010). The largest population consisted of several waves propagating toward the northwest at speeds of ~50–600 m/s. The second population consisted of two waves propagating almost due northward. Table 1 lists the characteristics of the waves observed on the night of the rocket launch, including their periods, phase speeds, propagation directions, and horizontal and vertical wavelengths. The mean azimuth for these waves is calculated and plotted as a direction vector in Figure 5, along with vectors representing the direction of the *F* region wind measured within the MSF event by the rocket (see section 5.2) and the direction to tropical storm Noel. Using reverse ray tracing and convective source modeling *Vadas and Crowley* [2010] find that the sources of waves propagating toward the northwest are likely thermospheric accelerations excited by dissipation of gravity waves associated with tropical storm Noel. Crowley et al. (submitted manuscript, 2010) argue that the smaller subset of northward propagating waves was probably launched from the southern auroral zone. So while it is possible that longer period waves unobservable to the TIDDBIT system were present in the ionosphere during the rocket flight, it can be confidently stated that the largest subset of waves having 15–90 min periods were associated with Tropical Storm Noel.

[26] By superposing all of the waves measured by TIDDBIT in a 3-D sense, taking account of their different periods, propagation directions, propagation speeds, and amplitudes, it is possible to reconstruct a 3-D image of the ionospheric perturbations over the radar, as depicted in Figure 6 (after Crowley et al., submitted manuscript, 2010). Figure 6 is deduced from the variation in O mode reflection height at 3.167 MHz and represents height perturbations in the isodensity surface of the bottomside ionosphere in the vicinity of Wallops Island near the time of the rocket launch. The reflection height variations are represented by grayscale shading, and contours are added to enhance the visibility of the variations. The interference of multiple waves traveling in different directions and with different wavelengths is what produces the "egg crate" pattern in Figure 6. Table 1 shows that each distinct wave detected by the TIDDBIT system has a different horizontal wavelength and phase speed. Since there is more than one wave contributing to the motion of the bottomside ionosphere, the mesoscale features shown in Figure 6 are not fixed, and likewise the pattern does not coherently propagate with a single speed. Instead Figure 6 should be interpreted as a composite snapshot of many inter-

Table 1. Waves Observed by the TIDDBIT Ionospheric Sounder During the Launch Window[a]

τ_r (min)	c_H (m/s)	Θ (°)	λ_H (km)	λ_z (km)
16	259	−27	255	201
16	180	−29	176	146
18	229	−15	248	166
18	168	−15	181	127
20	160	3	192	110
20	151	−3	182	108
36	263	−48	568	167
45	592	−56	1600	564
45	372	−27	1006	248
60	479	−20	1725	352

[a]The first column gives the wave period in minutes, the second column shows the horizontal phase speed, the third column is the wave azimuth, and the fourth and fifth columns give the horizontal and vertical wavelengths. The vertical wavelengths are estimated from model winds, as described in *Vadas and Crowley* [2010].

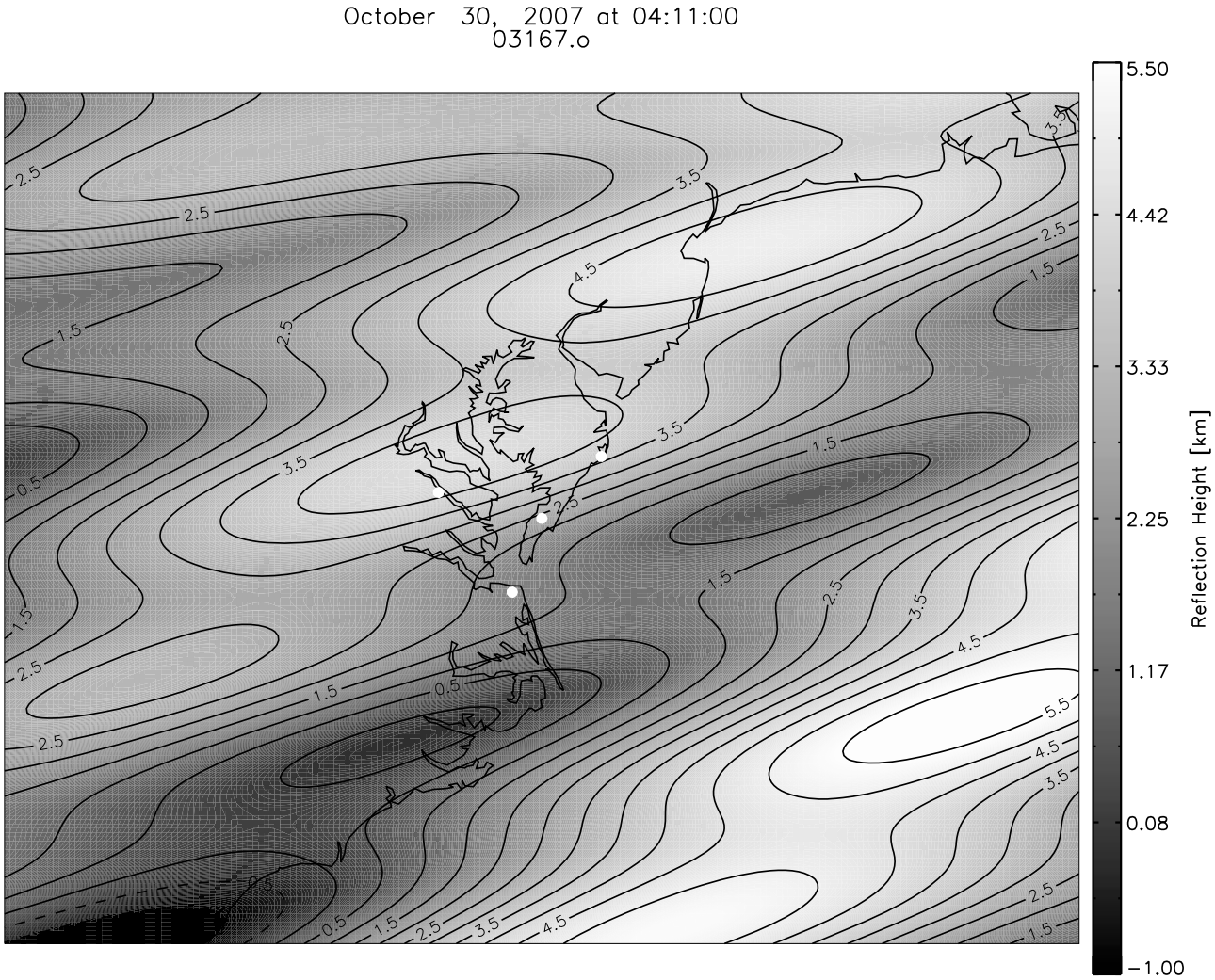

Figure 6. Contour plot from the TIDDBIT system showing the wavelike corrugations in the ionosphere over Wallops Island coincident with the rocket flight. The contours and grayscale show the deviation in reflection height for an incident O mode wave at 3.167 MHz. The height perturbations for each wave are obtained by integrating Doppler shifts as a function of time for each wave period. The effect of all the waves is summed while incorporating their different phases, wavelengths, and velocities. Large amplitude and long period waves produce the largest perturbations, which are therefore more noticeable in the plot than their shorter period, smaller amplitude counterparts.

acting wave components near the time of the rocket launch, just like a snapshot of the surface of the ocean. In practice, this pattern will be constantly changing.

[27] The four white dots in Figure 6 show the locations of the three transmitters and the centrally located receiver from which these measurements were deduced. The propagation paths monitored by the TIDDBIT system would be represented in Figure 6 by three line segments extending from the vertices of the largest triangle of white dots toward the centrally located dot. The midpoints of these line segments are the approximate locations where the vertical motions of the ionosphere are measured by the system.

[28] In the region surrounding Wallops Island, the measured height perturbations were less than about ±10 km on the night of the rocket experiment. The "egg crate" pattern in Figure 6 provides many individual locations from which specular reflection of radio signals could occur and which might explain the occurrence of range spread *F*, due to overlapping discrete HF radio reflections from different locations within the field of view of the ground based ionosondes, in agreement with the data shown in Figures 3 and 4. This concept will be explored further in section 6.

[29] Note from Table 1 that each distinct wave detected by the TIDDBIT system has a different horizontal wavelength and phase speed. Since there is more than one wave contributing to the motion of the bottomside ionosphere, the features shown in Figure 6 are not coherently propagating with a single speed. Instead Figure 6 should be interpreted as a spatial composite snapshot of many interacting wave components propagating overhead near the time of the rocket launch. With this interpretation, the TIDDBIT data are seen to be consistent with the idea of the ionosonde and dynasonde observing multiple reflections at each frequency step from different ranges over their respective fields of view. When

these distinct traces created by multipath reflections overlap on a standard ionogram they create the signatures we identify as MSF.

4.4. Scintillation Data Trends

[30] The 244 MHz scintillation detectors at Martha's Vineyard were positioned to look over Wallops Island along the azimuth of the rocket flight at an elevation angle of 30°, resulting in a relatively long slant path through the ionosphere. Because scintillations result from the total density fluctuation integrated along the raypath, the experiment geometry provided good sensitivity to irregularities occurring throughout the *F* region at spatial scales less than ~1 km. During several weeks of nighttime operation prior to the rocket launch these receivers detected only very weak intermittent variations in the S4 index. These observations were found to be uncorrelated with observations of spread *F* on the Wallops digisonde and probably resulted from variations in the modulated power of the satellite signals being monitored. On the night of the launch the maximum S4 index never exceeded 0.1, the same as the background variations on nights when MSF was not observed. Altogether there are nighttime scintillation data available from the *F* region over Wallops Island for a period of more than three weeks during which simultaneous digisonde data were available. Throughout this period there were no significant S4 index differences between nights with and without spread *F*.

[31] The absence of correlated spread *F* observations and VHF scintillations at midlatitudes is not surprising given the different sensitivity of the respective measurement techniques to different scale sizes. The spread *F* phenomenon observed by HF vertical sounding results from density structures greater than 10 km in wavelength, while the Fresnel filtering effect on VHF amplitude scintillations limits the contributions of irregularities greater than a Fresnel length $(2\lambda Z)^{1/2}$, where λ is the wavelength of the radio wave and Z is the effective distance to the irregularities. For this experiment $\lambda = 1.2$ m and $Z \sim 600$ km, giving a Fresnel scale of 1.2 km; larger scale sizes have no effect on the observed amplitude fluctuations of the signal. The absence of scintillations therefore implies the absence of significant plasma density structure at km and smaller scale sizes.

[32] Midlatitude spread *F* events are typically associated with TIDs and gravity wave-driven mesoscale (10–100 km) density perturbations. Smaller-scale propagating wave perturbations that might cause scintillations are effectively filtered out in the lower thermosphere and do not reach *F* region heights. Thus, the irregularities responsible for radio wave scintillations are usually generated locally in the *F* region as a result of instability processes that lead to the cascade of energy from larger to smaller scales. The gradients commonly associated with TIDs and other midlatitude wave phenomena are too weak to drive drift wave instabilities and subsequent short wavelength perturbations. However, strong midlatitude scintillations have been observed during the main phase of major magnetic storms when typical electron densities and gradients may be enhanced by an order of magnitude or more [*Basu et al.*, 2005]. Although Kp was enhanced during the periods considered here, no major storms were in progress, nor were sharp electron density gradients observed. The lack of small scale density irregularities and scintillation coincident with the observed MSF signatures is a new result that has not been measured or reported previously. It is confirmed in our experiment by the in situ plasma density measurements, as we show below.

4.5. In Situ Data During the MSF Event

[33] As the rocket flew through the *F* region it measured the plasma density, neutral wind and electric field over the range of altitudes where spread *F* signatures were observed on the digisonde and dynasonde. This section presents these data for comparison with the ground-based data shown above. In interpreting these data it is important to remember that the rocket spent only a few minutes within the spread *F* region as it moved upward and toward the southeast at ~400–800 m/s. The horizontal component of the rocket's velocity was nearly constant throughout the spread *F* region, but its vertical velocity continually decreased as the rocket approached apogee at 394 km.

[34] Measurements made by the rocket must therefore be considered "snapshots" of the local medium; the rocket observations cannot provide any data on the long-term temporal evolution of the medium during the spread *F* event. Furthermore, a single rocket interrogates only one event, so there are no statistics to indicate whether the behavior observed is typical. Despite these limitations, the rocket data provide a detailed view of parameters that cannot be measured from the ground, such as the vector electric field and neutral winds.

4.6. Plasma Density Data

[35] The electron density data are shown in Figure 7, with uncertainties in the absolute values on the order of 20%. The plasma density data within the sporadic *E* layer in Figure 7 are from the ionosonde measurements just prior to the rocket launch. The in situ plasma density data from the *F* region rocket measurements have been combined with these lower altitude ionosonde measurements to obtain the composite density profile shown in Figure 7. Values from the IRI model for conditions on the launch night have been scaled to fill in the plasma density in the *E*-*F* valley region by matching the model values to both the *F* region rocket data above and the ionosonde data below. The matching was accomplished by scaling the IRI model data in the valley region by a small constant factor to match the end points of the DCP and digisonde data.

[36] The DC probe (DCP) data presented in Figure 7 were sampled with high temporal resolution to reveal small-scale features, but the raw data were marginally contaminated by oscillations of the payload ground potential attributed to charge collection by an open umbilical connector moving in and out of rocket's wake. These periodic errant data points have been manually identified and removed during analysis and are not shown in Figure 7. The resolution of the DCP is ~2.3×10^4 cm^{-3} for this experiment, which is sufficient to clearly resolve the minimum between the double *F* peak features.

[37] The rocket-borne impedance probe (PIP) operated in two modes: tracking mode, where the instrument locks on and tracks the plasma upper hybrid frequency, and sweeping mode, where the instrument measures the antenna impedance over a range of frequencies. During the flight experiment, the tracking mode locked onto the upper hybrid frequency for a short time in the *F* region on the upleg portion of the flight, providing an absolute in-flight calibration between the DCP and the PIP instruments.

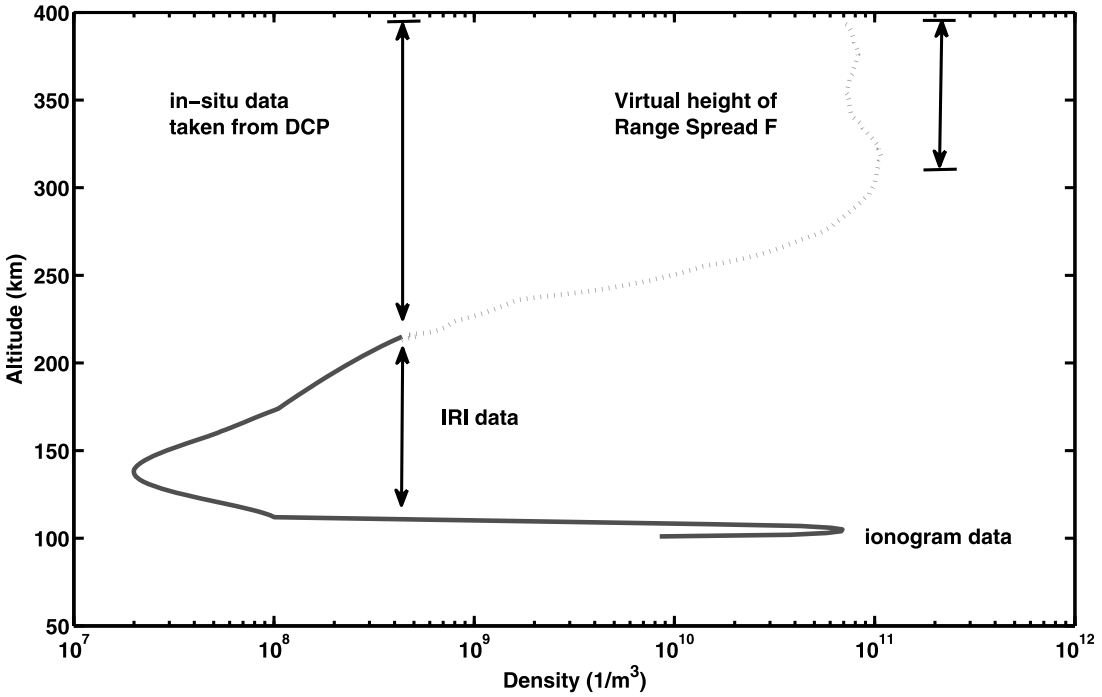

Figure 7. *F* region plasma density data from the fixed-bias DCP, normalized to the absolute measurements from the swept frequency impedance probe. The *E* region data are from the digisonde, and the *E*-*F* valley region is filled in with data scaled from the IRI model for the time and date of the rocket flight. Note the presence of a secondary *F* peak near 375 km.

[38] The *F* region electron density data presented in Figure 7 are the DCP relative density measurements after normalization to the absolute density derived from the interval in which the PIP was locked to the local upper hybrid resonance frequency. The region between ~310 and 390 km corresponds to the heights at which spread *F* was simultaneously detected on the ionograms and also to an apparent double *F* peak which will be discussed in more detail later. Note that the *F* region density profile is quite smooth; there are no small-scale plasma density fluctuations evident in the in situ data.

4.7. Neutral Wind Measurements

[39] The pressure variations measured by the HATI instrument are used to calculate wind direction and amplitude. The pressure ratio in two diametrically opposed chambers within the sensor is combined with the known rocket velocity and orientation to calculate the horizontal wind magnitude, as described by *Hanson et al.* [1992]. Although this reference applies specifically to satellite applications, it provides a good mathematical interpretation relating the chamber pressure within the instrument to the external atmospheric pressure and the arrival angle of the neutral gas. Throughout the flight the attitude control system maintained the alignment of the rocket to within 5° of its velocity vector. As in the satellite version of the neutral wind instrument, the inherently 2-D measurement transverse to the direction of motion is related to a unique wind direction. In the rocket scenario, we make the assumption that the vertical component of the wind is negligible in comparison to the horizontal components, thereby allowing an estimate of the horizontal wind to be obtained from the rocket measurements. If a portion of the neutral wind perturbation is caused by gravity waves, this is a good assumption if the vertical wavelength is much smaller than the horizontal wavelength [*Hines*, 1960]. For those gravity waves that can propagate to ~400 km altitude this is a good approximation (S. L. Vadas and G. Crowley, Thermospheric wind and density perturbations created by the gravity waves observed by the ionospheric TIDDBIT sounder at the bottomside of the F layer, submitted to *Journal of Geophysical Research*, 2010).

[40] Figure 8a shows the horizontal wind magnitude obtained from this procedure, while Figure 8b shows the direction. The corotation velocity has been removed prior to plotting. The error bars shown in Figure 8 are calculated by applying the analysis procedure to the unsmoothed raw data; thus, they represent uncertainties due to the noise level from the electronics, as well as signals induced by short-lived payload transients such as those produced by the attitude control nozzles. The wind direction shown in Figure 8 is nearly constant toward the north-northwest over the short duration of the rocket flight, but the amplitude varies from a maximum of ~130 m/s near the *F* peak to a value of ~30 m/s in the topside. Note that this observed neutral wind amplitude is not unreasonable for the oscillating horizontal component of a gravity wave-driven neutral wind perturbation, as we will discuss in detail later.

4.8. Electric Field Measurements

[41] The DC electric field measurements from the rocket flight are shown in Figure 9. These measurements use the floating double-probe technique [*Fahleson et al.*, 1970] with the assumption that the component of the electric field parallel to the geomagnetic field in the midlatitude *F* region

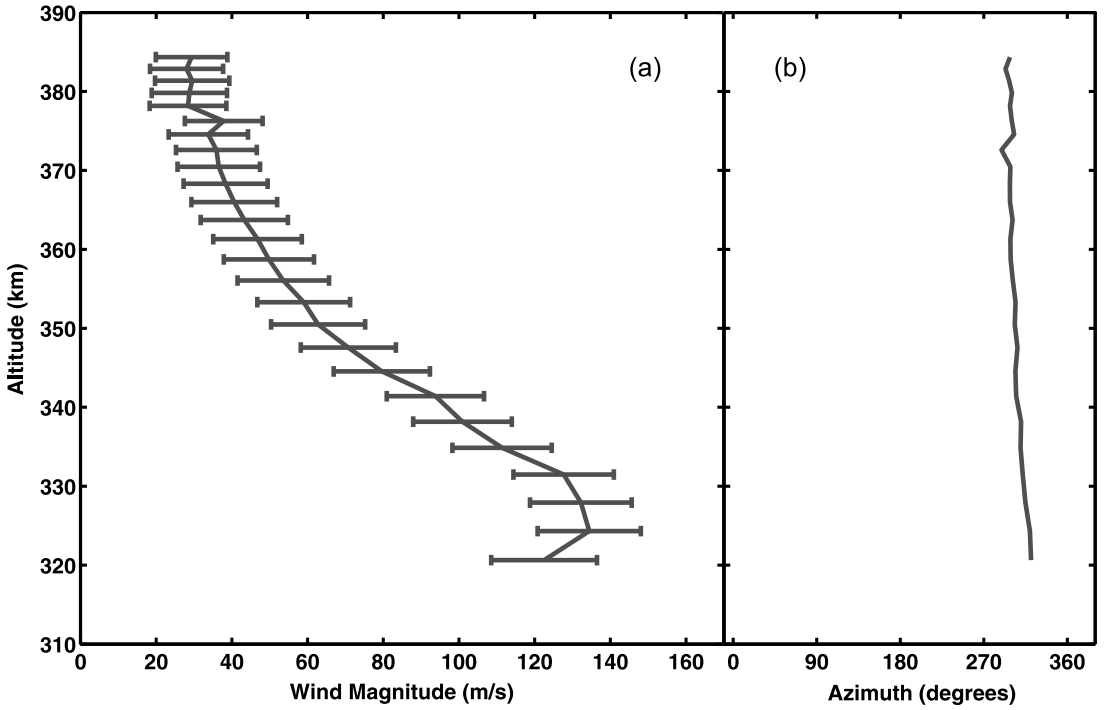

Figure 8. *F* region neutral wind (a) magnitude and (b) direction in the Earth-fixed reference frame during the midlatitude spread *F* event shown in Figure 1.

is zero. The fields caused by corotation and by the rocket's motion perpendicular to the magnetic field ($\mathbf{v} \times \mathbf{B}$) have been subtracted, and the resultant electric field vector is shown after rotation into the Earth frame, assuming $\mathbf{E} \cdot \mathbf{B} = 0$. The uncertainty in these measurements due to channel noise is ~0.2 mV/m. Figure 9 shows the electric field measurements in the geographic frame of reference, so they may be compared with the wind measurements more easily. At low *F* region altitudes the field is southeastward, but near apogee it is substantially larger and toward the northwest.

5. Derived Data Products

5.1. Reflected Ray Paths

[42] The ionograms from the digisonde system at Wallops Island show continuous O mode traces indicative of normal

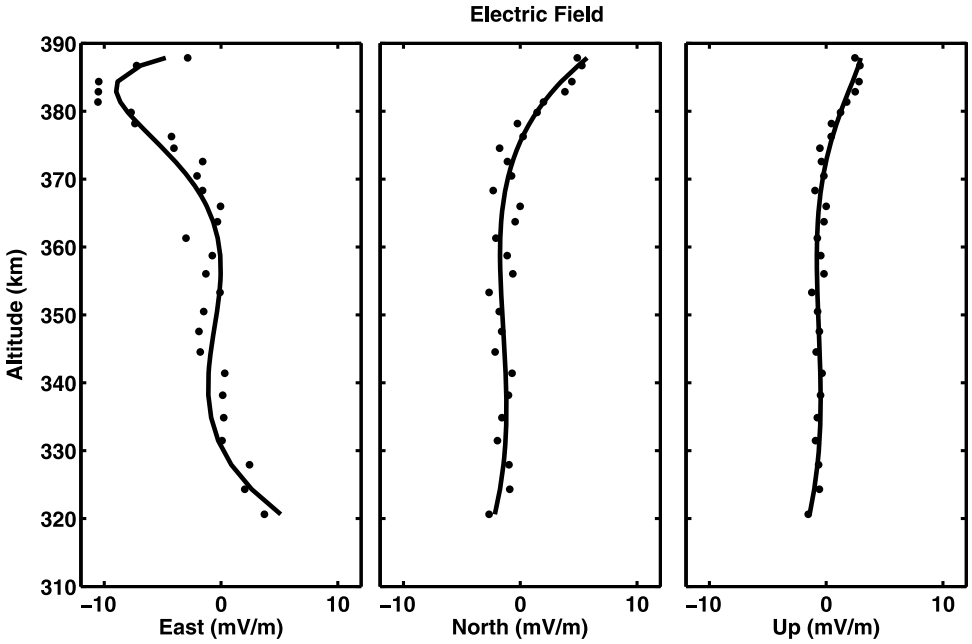

Figure 9. *F* region electric field in the MS*F* region, shown in the geographic frame of reference with the corotation field removed.

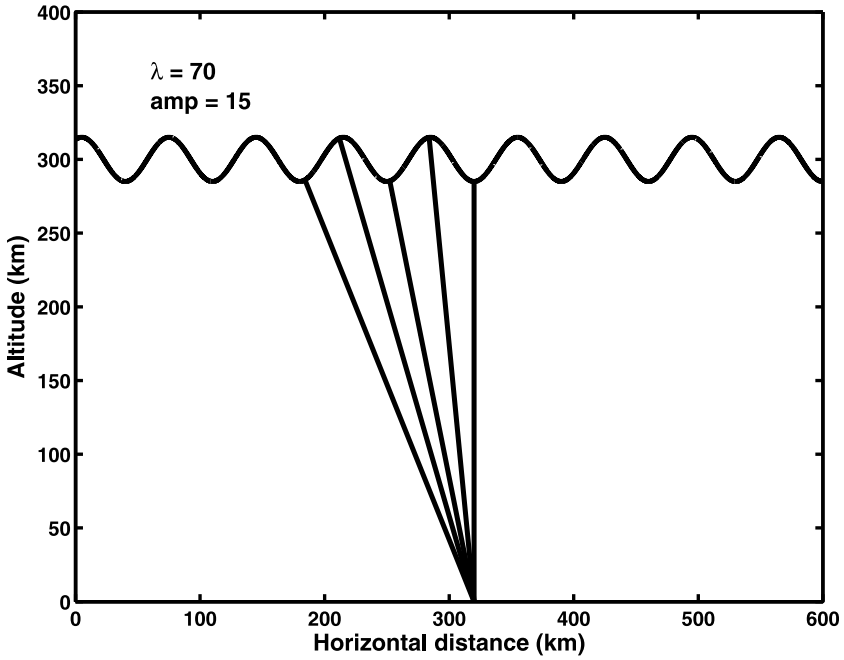

Figure 10. Simple geometric model of a corrugated bottomside ionosphere for a particular periodic horizontal structure length and altitude displacement. The sinusoidal feature represents an assumed isodensity contour, and the straight lines represent raypaths at normal incidence within the field of view of the ionosonde.

spread *F* signatures, such as those studied by *Bhaneja et al.* [2009]. The phase-sensitive dynasonde data in Figure 4 reveal that this particular spread *F* feature is comprised of several discrete, overlapping O mode traces. These data are consistent with an ionosphere that has multiple critical reflection points within the radar's field of view, like those shown in Figure 6. The bottomside *F* region structures create a situation in which multiple rays lying within the beam of the ionosonde produce backscatter at the same frequency. Because the path length for each of these reflected rays is different, the result is overlapping traces on the ionogram, which produce a spread *F* type signature. This interpretation accounts for the spreading seen in the ionograms. The digisonde system fails to resolve these as separate traces, but the more sensitive dynasonde can do so. The occurrence of multiple distinct traces implies that a wavy or corrugated structure exists in the bottomside ionosphere, with density scale sizes that are smaller than the footprint of the radar systems in the bottomside *F* region. Such structures may be created by gravity waves lifting some regions of ionization while lowering others, as suggested by *Bowman* [1991] and shown in Figure 6.

[43] Figure 10 shows a plot to illustrate how a corrugated bottomside *F* region can produce HF echoes from different ranges. The example shown assumes a wave-like structure with a 70 km horizontal scale length and a vertical displacement amplitude of 15 km in plasma medium. The sinusoidal curve represents an isodensity contour for the idealized bottomside density structures, and the straight lines represent the rays transmitted from a ground-based ionosonde to the ionosphere. Nighttime conditions are assumed so the underlying *E* region density is small; this allows us to ignore variations from straight line ray propagation at low altitudes. Reflection of the incident rays occurs where they are perpendicular to the slope of the isodensity structure.

[44] Path differences less than ~29 km are not well resolved by the standard Wallops Island digisonde and are therefore interpreted as MSF. The more sensitive dynasonde data in Figure 4 show that the path length differences between discrete echoes were on average ~11–12 km during the experiment. From inspection of Figure 10, it is apparent that as the horizontal wavelengths and to a lesser extent the vertical displacements become larger, the virtual path length differences increase and are more readily resolved in the standard ionograms. Simple geometry shows that density perturbations with horizontal scale lengths less than ~80–100 km will lead to path length differences that are poorly resolved by a standard ionosonde at all amplitudes. Assuming that upward/downward motion of the *F* region created by gravity waves produces plasma density perturbations at lower *F* region heights, the clear implication is that shorter horizontal wavelengths are more likely to produce midlatitude spread *F* signatures.

5.2. Plasma Drifts

[45] Examination of the wind and electric field data in Figures 8 and 9 reveals that $\mathbf{E} + \mathbf{u} \times \mathbf{B} \neq 0$ in the MSF region, so the winds and electric fields observed during the rocket mission are not balanced. We interpret this as evidence that the electric fields measured in the *F* region may be mapped along the geomagnetic field from *E* region altitudes, as discussed in more detail later. Figure 11d shows the magnitude of this expression. In light of the TID activity from the auroral and tropical disturbances prior to the onset of MSF (Crowley et al., submitted manuscript, 2010), it seems likely that the observed *F* region wind is due to a

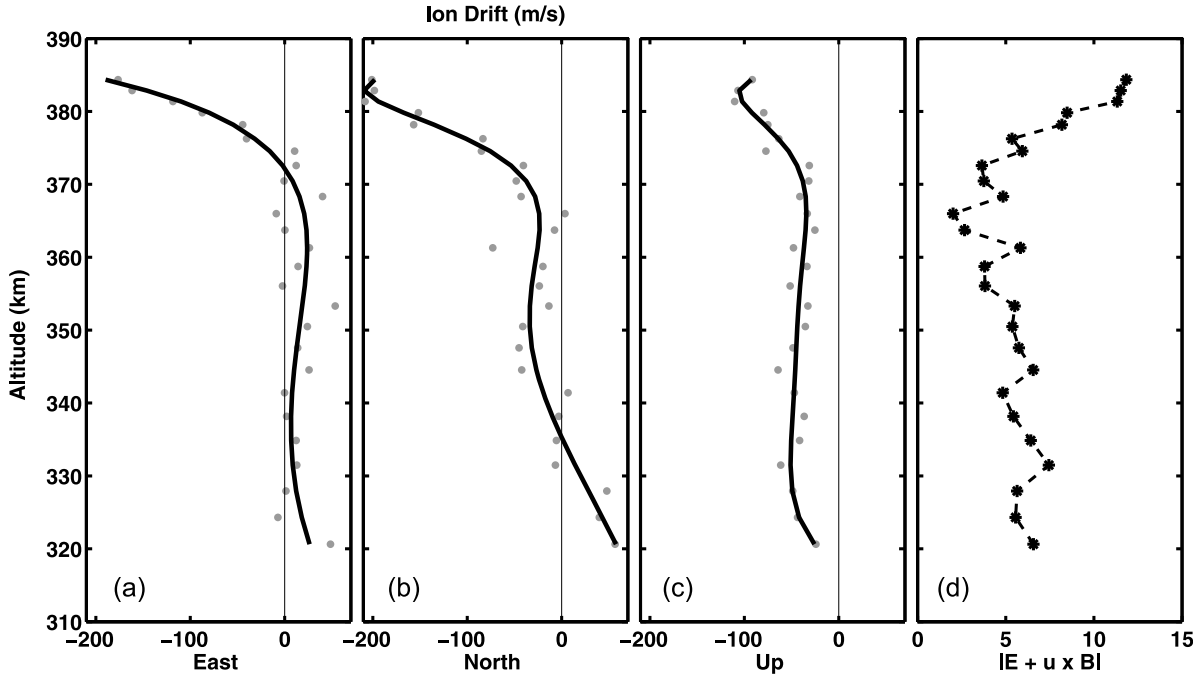

Figure 11. (a–c) The calculated steady state ion drift in geographic coordinates, based on the measured wind and electric field in the *F* region. (d) The calculated value of $\mathbf{E} + \mathbf{u} \times \mathbf{B}$ in mV/m, using *F* region measurements from the rocket.

transient or propagating perturbation superimposed on the normal tidal wind system. The ion drift necessary to produce a quasi-steady state solution to the momentum equation can be calculated from the measured wind and field data; this is plotted in Figures 11a–11c. In the altitude range (350–400 km) corresponding to the height of the spread *F* condition the ion drift changes from southward to strongly southwestward. The calculated ion drift is consistently downward throughout the nighttime *F* region, as expected.

5.3. Instability Growth Rates

[46] Many previous authors have invoked instabilities in attempting to explain MSF and other midlatitude irregularities observed by ground-based instrumentation [*Perkins*, 1973; *Behnke*, 1979; *Hanson and Johnson*, 1992; *Kelley et al.*, 2000; *Cosgrove and Tsunoda*, 2004]. The space-based measurements from the HATI instrument indicate a neutral wind consistently in the northwest direction throughout the spread *F* region, and the electric field measurements from the VEFI instrument indicate an electric field in the south–west direction. These directions are both consistent with the required geometry for the Perkins instability. We have calculated the maximum growth rates for the conditions of our experiment using the expressions derived by *Perkins* [1973] for both the measured wind and electric field source drivers. Figure 12 shows these calculated growth rates to be very low, about $5 \times 10^{-4}\ s^{-1}$ at the altitudes where range spreading is observed. This implies an e-fold growth time of at least 30 min, which is not consistent with the sudden onset of spread *F* seen repeatedly during the experiment observations up to and including the night of the rocket launch. On all nights when midlatitude spread *F* appeared during our experiment window, the ionograms typically evolved from completely normal to fully disturbed in periods of only ~5–10 min.

[47] *Cosgrove and Tsunoda* [2004] propose a theory in which electric fields produced locally in the *E* region map to the *F* region, creating a coupled *E*-*F* region plasma instability with a growth rate substantially larger than the Perkins growth rate. There is no closed form solution for the growth rate of this instability, so unfortunately we cannot compare our observations to this theory directly. However, a key element of this hypothesis is the formation of polarization electric fields in a highly conductive *E* region, such as one with a substantial sporadic *E* layer. As shown in the composite plasma density profile in Figure 7, this condition likely existed during our rocket experiment, assuming that the sporadic *E* layer extended far enough to the northwest from Wallops Island to intersect the flux tubes connecting to the *F* region over the ionosonde. Horizontal currents in this layer could create large polarization fields if the plasma density in the layer was not uniform.

[48] The plasma density profile shown in Figure 7 yields the conductivity profiles shown in Figure 13 when combined with typical neutral atmosphere temperatures and densities from the MSIS model for conditions appropriate for the launch date and time. The direct conductivity is shown on the top scale, and the Hall and Pedersen conductivities are given on the bottom axis. Both the Hall and Pedersen conductivities are quite large within the sporadic *E* layer.

[49] To more closely examine the coupled *E*-*F* region hypothesis, it is helpful to rotate the rocket observations into a magnetic coordinate system. We can then examine the variations of the parameters measured in situ as a function of distance traveled by the rocket perpendicular to the geomagnetic field. Figure 14 shows the result for the measured

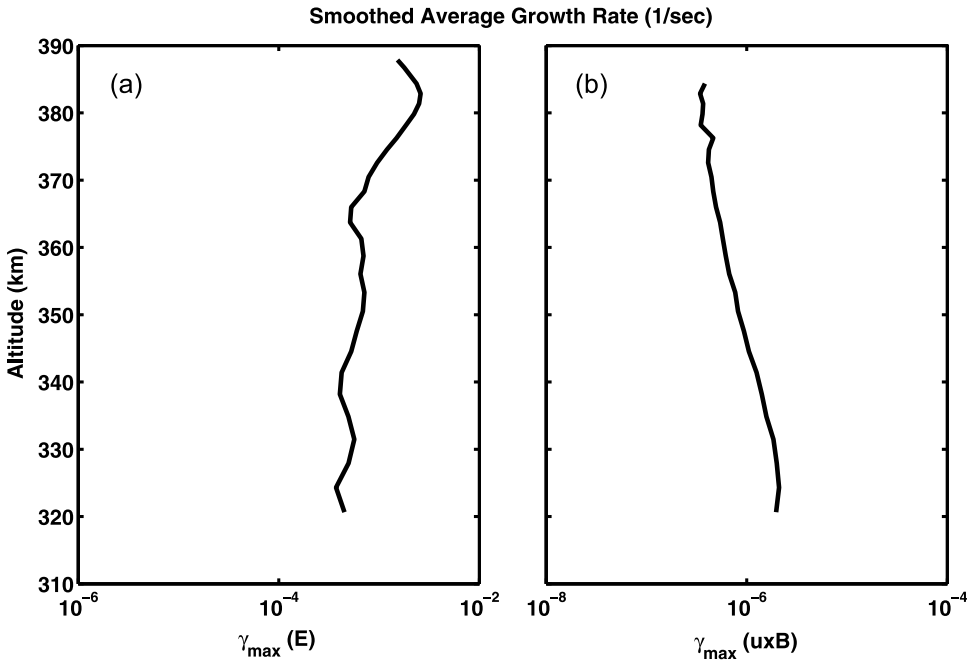

Figure 12. Maximum growth rate as defined by *Perkins* [1973] using (a) E and (b) $-\mathbf{u} \times \mathbf{B}$.

F region plasma density, electric field, neutral wind, and calculated ion drift. Of particular interest is the electric field shown in the second panel, which increases along the rocket's trajectory. Coincident with the observation of the secondary *F* region peak the westward component of the electric field begins to increase substantially, and it continues to do so all the way to apogee (the right edge of the plot). The prevailing wind has the opposite behavior; it is large at lower altitudes

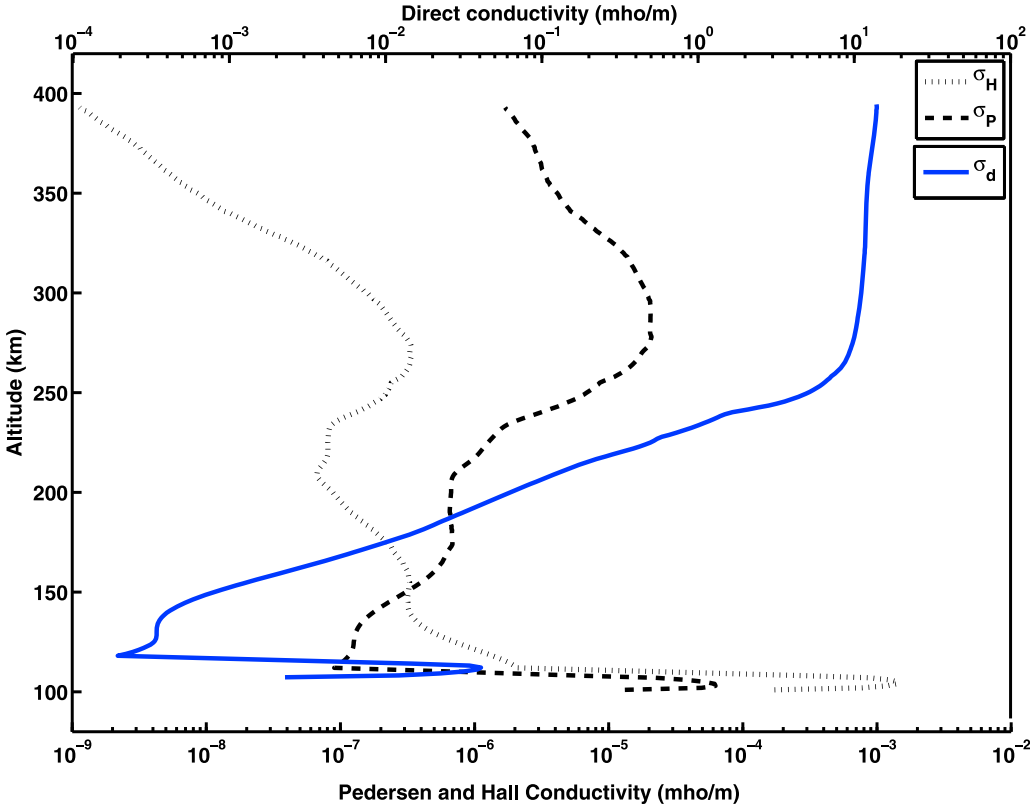

Figure 13. Conductivity profile obtained using plasma density data from the rocket and digisonde, in combination with model values from the MSIS and IRI models for conditions prevailing at the time of the launch.

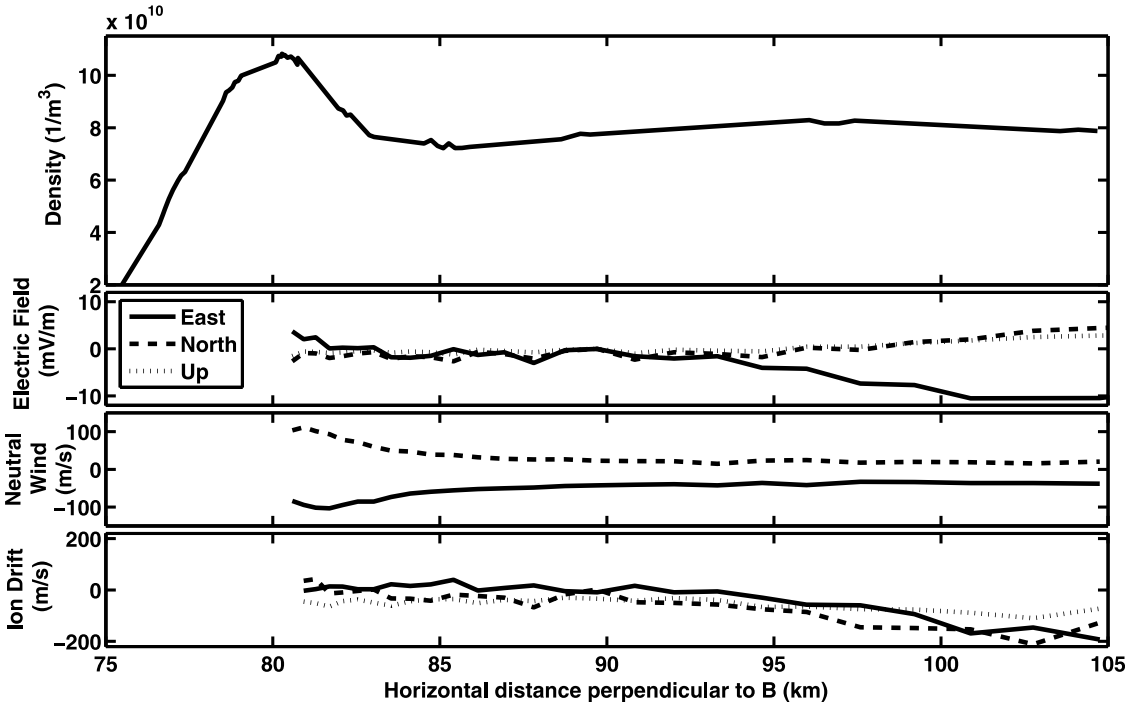

Figure 14. Measured electric field, neutral wind, and plasma density plotted as functions of the distance traveled by the rocket perpendicular to the magnetic field.

near the launch site and becomes smaller as the rocket moves to the southeast, upward, and away from Wallops Island.

6. Discussion

[50] The data shown in Figures 7, 8, and 9 are the first simultaneous measurements of the wind, electric field, and plasma density within a region of active MSF. Although the directions of the electric field and neutral wind measured by the rocket in the *F* region are consistent with the required geometry for the instability described by *Perkins* [1973], the instability growth rates calculated from the in situ measurements are on the order of a few times 10^{-4} s^{-1} at the height of the MSF region; thus, the Perkins instability would require more than half an hour to grow and form a spread *F* condition. In contrast, the ionosonde observations on the night of the launch and on other nights during the launch window show that the onset of MSF conditions is very rapid and therefore not compatible with these slow growth rates. The preponderance of gravity waves measured simultaneously with spread *F* observations suggests that no instability is necessary to produce the phenomenon observed on the night of the rocket launch, because the observations can be explained as a driven oscillation rather than an instability. The smooth density profile measured by the rocket on scales less than a few kilometers is consistent with this interpretation and also with the lack of scintillation activity measured independently during the spread *F* event.

[51] Ionospheric structures are known to be produced directly by gravity waves [*Hooke*, 1968; *Klostermeyer*, 1972; *Vadas and Liu*, 2009]. *Bowman* [1990, 1991] speculates that MSF may result simply from wave-driven density perturbations of the bottomside *F* region ledge, possibly superimposed with a larger-scale horizontal gradient in the background density. The hypothesis is that a spread *F* condition is detected in ionograms when the incident radio waves are reflected from tilted surfaces in the ionosphere that are created by horizontal and vertical density gradients produced by gravity waves/TIDs. Our combined observations with the digisonde and dynasonde (Figures 3 and 4) together with TIDDBIT (Figure 6) prove this hypothesis by providing the first high-resolution data that simultaneously show both the classic spread ionogram signature and the discrete overlapping O mode traces that comprise it.

[52] The simple geometry depicted in Figure 10 can be used to imagine this scenario. The path lengths of the rays drawn in Figure 10 have different lengths, and the resulting echoes would appear at different heights when represented in a standard ionogram. The average range difference between the discrete traces observed in the dynasonde image in Figure 4 is ~11–12 km. Wave structures with small horizontal wavelengths and almost any amplitude will produce such small path length differences for incident rays within the field of view of the standard digisonde at Wallops Island. Larger amplitudes or longer horizontal wavelengths will produce longer path length differences. Since the MSF phenomenon in our experiment developed too quickly to be attributed to the Perkins instability, we are compelled to examine our data to identify a source for such small-scale structures in the ionospheric medium. The two most likely possibilities based on measurements by the rocket and radars are discussed in detail below.

[53] Crowley et al. (submitted manuscript, 2010) model the global thermosphere-ionosphere system and show that a small fraction of long-period, northward-propagating waves generated by auroral heating in the Southern Hemisphere might have reached Wallops Island at the time of the launch. Their model predicts simultaneous generation of large-scale

waves in both the northern and southern auroral regions, consistent with the increase in Kp observed several hours prior to the onset of spread *F* over Wallops Island. The long propagation distances imply that any waves from the northern auroral zone that could have reached Wallops Island in time to trigger the observed spread *F* would have periods of several hours, so they would be invisible to the TIDDBIT system. However, since the magnetic perturbations measured at Fort Churchill (and presented in Figure 1) show significant currents induced 3–6 h prior to the event, the northern auroral source must be considered plausible for the MSF we observe. On the other hand, waves from the southern aurora would not reach Wallops Island until about the time of the rocket launch (0412 UT), well after the onset of the spread *F* condition.

[54] The other source of northward propagating waves on the night of the rocket experiment was Tropical Storm Noel in the Caribbean. GOES satellite imagery coupled with knowledge of the temperature at the tropopause confirm that many deep convective plumes overshot the tropopause (i.e., had cooler temperatures than the tropopause) within this storm a few hours prior to the rocket launch [*Vadas and Crowley*, 2010]. Overshooting convective plumes generate gravity waves as fluid is pushed upward into the stably stratified stratosphere. *Vadas and Crowley* [2010] describe a model that calculates the gravity waves excited by such events; it has been validated via comparison with the amplitudes, wavelengths, and periods of the concentric rings in the OH airglow layer produced by an overshooting convective plume [*Vadas et al.*, 2009]. Using this approach, *Vadas and Crowley* [2010] model the gravity waves excited by the overshooting convective plumes in Tropical Storm Noel, using Convective Available Potential Energy (CAPE) maps to determine the plume updraft velocities. Ray tracing is used to map these "primary" gravity waves into the thermosphere. They find that the cohort of these primary waves that reach the bottomside of the *F* layer do so ~1000 km southeast of Wallops Island, due to their steep propagation angle and wind/dissipative filtering.

[55] *Vadas and Crowley* [2010] also find that the dissipation of many of these gravity waves at altitudes near ~140 km creates thermospheric accelerations that excite "secondary" gravity waves with horizontal wavelengths ranging from ~100 to several thousands of km. These secondary gravity waves have different spectral properties than the primary gravity waves because the neutral density scale height is much larger in the thermosphere; this difference allows many of the secondary gravity waves that have large vertical wavelengths to propagate up to altitudes of ~300–420 km [*Vadas and Liu*, 2009].

[56] The TIDDBIT radar data in Table 1 and Figure 6 show that the bottomside ionosphere was populated by numerous gravity waves on the night of the rocket experiment. The in situ data reveal the instantaneous wind magnitude and direction in the topside *F* region over a time period much shorter than the TIDDBIT radar data set. It is quite significant that the direction of the neutral wind measured by the rocket in the topside ionosphere is in good agreement with the direction of wave propagation measured in the lower *F* region by the TIDDBIT system. This observation fits the expected relationship for gravity waves with periods less than a few hours. If the background tidal winds can be neglected, then the neutral wind perturbations are aligned with the direction of wave propagation [*Hines*, 1960]. Since the TIDDBIT waves are high frequency, and those TIDDBIT waves that can propagate up to altitudes greater than 400 km have azimuths of about −40° to −60° (Vadas and Crowley, submitted manuscript, 2010), this observation agrees well with the idea that some of the TIDDBIT waves propagated above 400 km and contributed to the neutral wind perturbations measured by HATI. Preliminary work using a dissipative gravity wave dispersion relation also suggests that the neutral wind perturbation amplitudes of the TIDDBIT waves approximately agree with the wind perturbation amplitudes measured by HATI (Vadas and Crowley, submitted manuscript, 2010).

[57] The digisonde data in Figure 3 show the spread *F* signature over Wallops Island coincident in time with the gravity waves observed by the TIDDBIT system. The more sensitive dynasonde data from the same time interval are shown in Figure 4; they resolve the spread *F* event into multiple discrete echo traces that overlap each other in the standard ionogram, thereby leading to the spread *F* signature. This experiment is the first time an MSF signature has been resolved by a separate radar system into discrete traces, confirming the hypothesis of *Bowman* [1990]. A simple geometric model of a corrugated bottomside ionosphere within the ionosonde's field of view (Figures 10) shows that the most likely scenario for producing such overlapping ionosonde echoes is one in which the horizontal structures in the plasma density across the ionosonde's field of view have scale lengths less than ~80 km for small vertical displacement amplitudes.

[58] Figure 6 shows that TIDDBIT detects corrugations in the bottomside ionosphere at the time of the launch. However, the horizontal scale lengths of the individual bottomside *F* region waves detected by the TIDDBIT radar are much longer than 80 km. A likely explanation of this difference is that the integration process employed by the radar introduces a bias toward longer wavelengths and larger amplitudes in the height perturbations deduced from the TIDDBIT data. In addition to the larger-scale waves evident in Figure 6, TIDDBIT also shows the presence of many smaller-scale and smaller-amplitude waves. Figure 6 shows bottomside features located to the southeast of Wallops Island that have vertical displacements of ~3 km over horizontal scale lengths of ~100–200 km. However, it seems possible that additional small vertical *F* region displacements caused by superposition of smaller-scale gravity waves creates additional rippled plasma structures in the bottomside ionosphere, which subsequently produce the spread *F* signatures.

[59] Horizontal plasma density structures produced by gravity wave-driven ion-neutral coupling has been previously observed in satellite data at *F* region altitudes [*Earle et al.*, 2008]. However, in order for two or more interacting gravity waves to produce horizontal scale sizes significantly shorter than their individual wavelengths, they must be uncorrelated. Using reverse ray tracing during the launch period from 0400 to 0700 UT, *Vadas and Crowley* [2010] show that the TIDDBIT waves of interest here could not have originated directly from deep convection because of the large distance to tropical storm Noel and the small wave periods. However, the waves observed by the TIDDBIT system could be secondary waves created by thermospheric accelerations that are produced by the dissipation of the primary gravity waves excited by Noel near altitudes of 140 km.

[60] *Vadas and Crowley* [2010] show that although the total spatial extent of the accelerations produced by these primary waves is several thousand kilometers, the accelerations occur in small, uncorrelated patches that are 100–200 km in diameter over temporal scales of 10–15 min; this occurs because of the constructive/destructive interference of the primary gravity waves from more than a dozen independent convective plumes and clusters within the storm region. The secondary gravity waves excited by these accelerations are generally out of phase. If the observed TIDDBIT waves are indeed secondary gravity waves, then they are likely uncorrelated as well. We should therefore expect to see interference patterns generated by the superposition of these waves.

[61] The vertical displacements associated with the waves observed by the TIDDBIT system are relatively large. *Vadas and Crowley* [2010] show that the convection was very intense in tropical storm Noel, leading to gravity wave amplitudes ~10 times larger than for a typical single convective plume. Such large amplitudes cause the primary gravity waves to saturate at thermospheric altitudes ~50–70 km lower than waves from a typical convective plume. Since the secondary waves are excited at lower altitudes, they can grow to much larger amplitudes as they propagate upward through the thermosphere. Assuming an average neutral density scale height of ~15 km in the lower thermosphere, the excited secondary waves can then grow to amplitudes 5–10 times larger as they propagate into the *F* region of the ionosphere. The wave amplitudes at the bottomside of the *F* layer and at altitudes above ~400 km could become quite large because of this effect, but only for those waves that survive dissipative filtering. The neutral density perturbations of the secondary gravity waves from a single convective plume can be as large as 5% at altitudes of 400–420 km [*Vadas and Liu*, 2009]. Including wave saturation, the neutral density perturbations of the secondary gravity waves from Noel might be 5%–15% in this altitude range. If this scenario is correct, it lends further support to the idea that interference from multiple waves may have occurred over the rocket flight path and produced the observed *F* region density perturbations.

[62] The *F* region data from the rocket experiment are shown in Figures 7–9. They reveal a smooth ionospheric density profile with no discernable small-scale (subkilometer) structure. The neutral wind in the *F* region is steadily toward the northwest for the duration of the rocket flight, in excellent agreement with the average propagation direction of the waves observed by the TIDDBIT system. The azimuth of the wind is reasonably constant throughout the topside *F* region, ranging from ~320° near 320 km altitude to ~300° at 385 km. The wind amplitude decreases from ~130 m/s to only ~30 m/s over the same altitude range. Since the diurnal tidal amplitude does not change appreciably with altitude above ~200 km, the observed wind maximum is most likely not due to tides.

[63] There are a number of quantitative reasons supporting the idea that the wind field measured by the rocket is at least partly due to the horizontal wind perturbations of several of the gravity waves detected by the TIDDBIT radar system. First, the horizontal wind perturbation of a high-frequency gravity wave is in the same direction as its propagation vector. Most of the waves observed by TIDDBIT that have large enough sound speeds to reach 400 km altitude are propagating northwestward, in a direction very similar to the wind measured in situ. Second, the rapid decay with altitude expected for a gravity wave above ~300 km is consistent with the behavior of the measured wind velocity profile [*Vadas*, 2007]. We note that the neutral scale height is typically ~45–90 km at topside *F* region altitudes, and the observed wind amplitude decays by one e-fold over ~46 km. Finally, the measured winds appear to asymptotically approach a value of ~30 m/s above ~370 km in a direction opposite to the expected tidal wind, which is estimated by *Vadas and Crowley* [2010] to be ~35 m/s at this altitude. Thus, the amplitude of the large-scale wave perturbation necessary to match the measurements is about 30 + 35 = 65 m/s toward the northwest.

[64] These perturbation amplitudes are in agreement with the findings of *Vadas and Liu* [2009], who show that large-scale secondary gravity waves with horizontal wavelengths of ~2000 km have neutral density perturbations of ~5% that are constant with altitude above 300 km. The waves in this study have horizontal wind perturbations of ~50 m/s. Of the four large-scale gravity waves observed in our experiment and listed in Table 1, the wave with $\lambda_H = 1600$ has an azimuth of ~304°, which is quite close to the wind azimuth measured by the rocket at 370 km. The large vertical wavelength of this wave ($\lambda_z \sim 564$ km) would produce a wind perturbation that would appear to be relatively constant over a large altitude range.

[65] From Figure 6c of *Vadas* [2007], a gravity wave can have a dissipation altitude above 300 km if its horizontal wavelength is between 250 and 650 km. The dissipation altitude is defined as the altitude where a gravity wave's amplitude is maximum. Only one of the gravity waves from Table 1 ($\lambda_H = 568$ km) has the required horizontal wavelength to reach such high altitudes. The measured azimuth of this wave is 312°, in good agreement with the wind azimuth measured by the rocket at the altitude of the peak wind speed. Some of the other gravity waves measured by the TIDDBIT system might also contribute to the wind at ~320 km altitude, although their shorter wavelengths suggest that their amplitudes likely peak below 310 km. Waves with horizontal wavelengths less than 200 km are unlikely to have appreciable amplitudes at these heights.

[66] Subtracting the high altitude measured wind (~30 m/s) from the maximum wind measured by the rocket (~130 m/s) yields a maximum horizontal wind amplitude of ~100 m/s. Assuming a maximum vertical displacement of ~6 km from Figure 6, Vadas and Crowley (submitted manuscript, 2010) estimate a horizontal wind perturbation of ~110 m/s at 320 km altitude for the wave with $\lambda_H = 568$ km, in excellent agreement with the ~100 m/s amplitude obtained from the rocket measurements.

[67] In summary, it is likely that the horizontal neutral wind measured by the rocket was created by the superposition of at least three waves: the diurnal tide, the large-scale TIDDBIT wave with $\lambda_H = 1600$ km, and the medium-scale TIDDBIT wave with $\lambda_H = 568$ km. These waves likely have uncorrelated phases, but without long-duration observations of the wave interactions in the topside ionosphere we cannot uniquely determine whether the pattern of their constructive and destructive interference in the topside *F* region matches the displacements of the plasma measured by the rocket, as revealed by the double *F* peak feature in Figure 7.

[68] The double *F* peak structure is one of the most interesting aspects of the rocket observations. On the basis of the

dynasonde data shown in Figure 4 and the simple geometry described in Figure 10, we surmise that the double *F* peak structure in the plasma density profile results from a vertical displacement of the *F* region over the distance scale traversed by the rocket between the observations of the peaks. However, since the rocket flew along a parabolic trajectory toward the southeast, we cannot unambiguously determine the scale size of the structure. In the time interval between measurement of the two peaks the rocket traveled upward a distance of ~55 km, horizontally a distance of ~30 km and perpendicular to the magnetic field a distance of only ~17 km.

[69] A short horizontal scale length is well matched to the ideal geometry for producing overlapping O mode traces on the ionograms, as shown by the geometry illustrated in Figure 10. For example, the average path length difference between the O mode traces resolved in Figure 4 is 11.6 km, and Figure 10 shows that the vertical ray and the ray adjacent to it are reflected from locations on the isodensity surface that are about half a wavelength apart at an altitude of ~300 km, assuming a small amplitude for the vertical displacement. For this type of small amplitude vertical displacement, the horizontal half wavelength of the feature would therefore be ~84 km, which is larger than the horizontal distance traveled by the rocket between the double *F* peaks, but significantly smaller than the horizontal wavelengths of the gravity waves that could propagate to these *F* region altitudes (as described above). We are therefore forced to conclude that if the features producing the multipath signatures on the ionograms arise from gravity waves at topside *F* region altitudes, then interference effects must occur between multiple uncorrelated waves to create the effects observed.

[70] The measurements show that the topside *F* region winds observed by the rocket are in good agreement with the TIDDBIT radar observations of medium to large-scale gravity waves propagating toward the northwest at lower *F* region altitudes. So far, we have argued that these gravity waves could produce relatively short scale length plasma structure through constructive and destructive interference of multiple waves at the altitudes where the spread *F* is observed, but an alternative mechanism is also possible. Gravity waves with horizontal wavelengths less than ~50 km are common at *E* region altitudes and are known to dissipate below ~120 km [*Oliver et al.*, 1997]. If such short-scale waves modulate the density within a sporadic *E* layer, the resulting large polarization electric fields would map along geomagnetic field lines to the *F* region and produce $\mathbf{E} \times \mathbf{B}$ drifts that could displace the plasma and produce *F* region density structures. The mapping of these fields occurs at the Alfvén speed, so the fields in the *E* and *F* regions communicate in about half a second. In contrast, for $\mathbf{E} \times \mathbf{B}$ ion drift speeds of 100 m/s, the *F* region plasma requires ~5–15 min to form measurable density structures over the scales observed in our experiment.

[71] As shown in Figure 14, the two *F* region plasma density maxima measured by the rocket are separated by only ~17 km as measured perpendicular to the geomagnetic field. If this structure is in fact oriented along adjacent flux tubes, it suggests a sharp uplift of the *F* layer, where the rocket traveled first through the ordinary *F* layer density peak, and later encountered the uplifted plasma. The altitude of the observed range spread *F* corresponds to this apparent region of uplifted plasma. As previously discussed, the range spreading observed in the ionogram is a manifestation of multipath associated with variations of the *F* layer altitude. On the basis of the presentation in Figure 14, it can be argued that the observed *F* layer altitude modulation may be the result of electric fields produced by the sporadic *E* layer interacting with a neutral disturbance, such as gravity waves. For example, if the vertical winds associated with a gravity wave modulate the altitude of a sporadic *E* layer relative to the vertical shear in the horizontal wind, then the different horizontal winds at the different layer altitudes will push the ions in different directions but will not affect the magnetized electrons (in the direction perpendicular to the magnetic field). The resulting differential charge motion can create a large polarization electric field [*Cosgrove and Tsunoda*, 2001, 2002a]. In this interpretation, the spread *F*, plasma uplift, and electric fields are an *E-F* region coupled response, such as described by *Tsunoda and Cosgrove* [2001], *Haldoupis et al.* [2003], *Cosgrove* [2007], and *Yokoyama et al.* [2009]. The rocket sees this uplifted plasma region as a second *F* peak displaced upward from the first, consistent with the data shown in Figure 7. This displacement occurs over a distance of only ~17 km perpendicular to B, which is easily short enough to produce the multipath signatures in the ionograms.

[72] In looking for the cause of the plasma uplift, we note first that the event involved electric fields in excess of 10 mV/m, which is quite large for midlatitudes. Examination of Figure 13 shows that the E region conductivity was also large because of the sporadic *E* layer, and Figure 14 reveals that the plasma velocity at higher altitudes is correlated with the electric field more than with the neutral wind. Because of the low ion-neutral collision frequency in the upper *F* region, winds mainly affect the plasma by pushing it along magnetic field lines, whereas electric fields operate through $\mathbf{E} \times \mathbf{B}$ drift. In addition, the ~17 km horizontal separation between density peaks when measured perpendicular to $\mathbf{B}$ and the similarly small horizontal scales over which the electric field varies suggest a viable alternative to the idea of larger scale gravity waves interfering to produce MSF on the night of the launch.

[73] Although Figure 14 appears to show variation of the wind over a 10 km horizontal scale, this occurs during a period when the rocket is ascending steeply, and more likely represents a variation with altitude as represented in Figure 7. The electric field is subject to no such ambiguity; since it maps essentially unattenuated along the magnetic field, its variation is invariably due to the movement of the rocket from one flux tube to another. The electric field may be generated anywhere along the field line, giving rise to the *E-F* coupling theories referred to earlier.

[74] It is virtually impossible for a 10 mV/m electric field variation to be generated by polarization of the *F* layer. For example, consider an *F* region with uniform wind $\mathbf{u}$ and uniform field line integrated conductivity $\sum_p$. The result is a uniform current $J_0 = \Sigma_p \mathbf{u} \times \mathbf{B}$ flowing through the *F* layer. If a 1-D modulation of the conductivity is introduced, then the response is a 1-D polarization electric field $\Delta\mathbf{E}$, which is determined by current continuity according to $\mathbf{J}_0 = (\Sigma_{p0} + \Delta\Sigma)(\mathbf{u} \times \mathbf{B} + \Delta\mathbf{E})$. Rearranging and solving for $\Delta\mathbf{E}$ gives

$$\Delta\mathbf{E} = (\Delta\Sigma\mathbf{u} \times \mathbf{B})/(\Sigma_{P0} + \Delta\Sigma). \quad (1)$$

Thus, even a 30% conductivity reduction ($\Delta\Sigma = -0.3$) requires a 470 m/s wind in the midlatitude *F* region to make $\Delta\mathbf{E}$ exceed

10 mV/m. These numbers are well outside of the bounds of the *F* region data shown in Figure 14. However, a number of previous studies have shown that 10 mV/m electric fields can be generated in sporadic *E* layers [e.g., *Haldoupis et al.*, 1996; *Shalimov et al.*, 1998; *Cosgrove and Tsunoda*, 2001, 2002a], so the field measured by the rocket in the *F* region was almost certainly generated at lower altitudes on the same flux tube.

[75] The sporadic *E* layer polarization mechanism can be far more effective than *F* region polarization because (1) it operates via an electrojet-like Cowling conductivity, (2) neutral wind disturbances can easily modulate the conductivity of the thin collisional layers, and (3) sporadic *E* layers are intrinsically unstable [*Cosgrove and Tsunoda*, 2002b]. There has not yet been a clear empirical example of an *F* layer effect caused by a sporadic *E* layer polarization, but such effects have been shown in simulations [*Cosgrove*, 2007; *Yokoyama et al.*, 2009]. For example, Figure 10 from *Cosgrove* [2007] shows a 10 mV/m electric field generated by an unstable sporadic *E* layer causing a sharp rise in the *F* layer altitude. Effects resulting from the sporadic *E* layer instability do not require a substantial neutral wind disturbance; but they are expected to conform to the geometry that maximizes the instability growth rate. The electric fields shown in Figure 14 do not match this orientation. However, the layer may be unstable in almost any orientation [*Cosgrove*, unpublished result], and almost any neutral wind disturbance will enforce a perturbation of the layer and cause a polarization electric field [e.g., *Cosgrove and Tsunoda*, 2002a].

[76] Assimilating all of these factors, a plausible scenario consistent with the spread F, electric fields, and double peaked density structure observed in the experiment described herein is as follows:

[77] 1. The dense undisturbed sporadic *E* layer observed prior to the initiation of spread *F* drifts to the north, clearing the view for the ionosonde to observe the spread F event, while simultaneously positioning itself on field lines that link to the portion of the *F* layer observed by the ionosonde.

[78] 2. Gravity waves modify the plasma density in the sporadic *E* layer and create an altitude and/or field line integrated conductivity modulation that becomes strongly polarized over relatively short horizontal scale lengths. This process may be aided by the sporadic *E* layer instability, albeit in a nonmaximal configuration.

[79] 3. The electric fields generated in the sporadic *E* layer map along field lines to the *F* layer, where they modulate the *F* layer altitude through the $\mathbf{E} \times \mathbf{B}$ drift. The resulting *F* layer structure displays a horizontal scale size derived from the scale size of the gravity waves that impact the sporadic *E* layer near 100 km in altitude. This ~17 km scale size is well in keeping with the expectations for gravity waves at 100 km in altitude but is inconsistent with both the TIDDBIT observations in the lower *F* region and the theoretical expectations for propagating gravity waves near ~300 km altitude.

[80] 4. The distortion of the *F* layer is a time-integrated effect, but the sporadic *E* layer may drift horizontally relative to the *F* layer so that at any instant in time, such as at the time of the rocket passing, the electric field is not well correlated with the *F* layer distortion. For example, a 10 mV/m electric field will require 5–15 min to displace the *F* region upward or downward by an amount consistent with our observations, but the electric field maps from the E region to the *F* region in less than a second.

[81] 5. The modulated bottomside *F* layer altitude leads to multipath of the ionosode signal, which manifests as range spread *F*. The combined rocket and radar observations presented here are consistent with the cause and effect scenario outlined above.

[82] In summary, we have described two different mechanisms by which *F* region plasma density structures could be created over horizontal scales appropriately sized to generate the multipath echoes observed by the digisonde and dynasonde during our experiment. The first requires that interference patterns be created by multiple interacting gravity waves in the *F* region, and the second involves upward mapping of electric fields produced in the E region. Our rocket experiment measures electric field and neutral wind signatures that do not rule out either mechanism and that demonstrate $\mathbf{E} + \mathbf{u} \times \mathbf{B} \neq 0$ at the altitude of the MSF. The fact that the wind and electric field are not self-consistent lends additional support to the idea that the electric field is produced in the *E* region, rather than locally. There are many more gravity waves present at *E* region altitudes than in the *F* region, due to the dissipative filtering effects described by *Vadas* [2007]. This is especially true of short wavelength waves, which simply do not propagate in the upper thermosphere. Thus the electric fields produced when these waves modulate sporadic *E* layers can have short scale lengths, consistent with our inference that short scales perturbations are more likely to produce MSF. The wavelengths of gravity waves that propagate to *F* region altitudes are much longer than the majority of those present at lower altitudes, and since the ions are unmagnetized at *F* region altitudes they can move perpendicular to the field lines in response to the winds and form density structures with scale sizes representative of the wave-induced motion.

[83] An important aspect of these behaviors is that there is no clear feedback path by which the local *F* region winds and mapped *E* region electric fields limit one another. The two sources of ion motion are independent, because they are driven by different, uncorrelated physical processes. Consequently, it is possible for both mechanisms to act simultaneously and independently. This may be happening in our particular MSF event.

7. Conclusion

[84] A joint radar and rocket project carried out at Wallops Island in late 2007 has provided a more complete picture of midlatitude spread *F* than has ever been available before. The single rocket experiment yields detailed information about only one event, so we cannot claim that our observations are typical of midlatitude spread *F* at all times and/or latitudes. However, for the particular MSF event studied here the combination of the in situ data from the rocket, ground-based radars, and scintillation monitors have produced a number of interesting new results.

[85] The standard ionograms taken during the experiment show typical spread *F* signatures, but for the first time a new high-resolution dynasonde system at Wallops Island resolves the spreading into six discrete echo traces separated in virtual range by an average of 11.6 km. This new finding confirms

the hypothesis by *Bowman* [1990] that horizontal variations in the bottomside plasma density produce overlapping echo traces in ionograms and create midlatitude spread F. Simultaneous 244 MHz scintillation measurements show no significant enhancements in the S4 index coincident with the spread *F* signatures, indicating a lack of plasma density structure at scales less than ~1 km within our MSF event.

[86] The instrumented rocket flown through the spread *F* event also shows no evidence of subkilometer plasma density or electric field structure, but detects a distinct double *F* peak. In the time interval between the observations of these two peaks the rocket travels ~55 km upward, ~30 km horizontally in a southeasterly direction, and only ~17 km perpendicular to the geomagnetic field. The neutral wind measured by the rocket in the topside *F* region is consistently toward the northwest, with a magnitude that drops from ~130 m/s at 330 km altitude to ~30 m/s at 380 km. The measured electric field varies from ~1 mV/m toward the southwest to ~8 mV/m toward the northwest over the same altitude range. The observed double *F* peak in the rocket data is likely caused by upward/downward displacement of adjacent regions in the ionosphere, which produce a corrugated bottomside *F* region ledge over the few hundred kilometer beam width of the ionosonde at these heights. This explanation is consistent with the vertical motions detected by the radar system during the rocket flight and with two different explanations for the bottomside structures:

[87] 1. Interference patterns generated by the interaction of tides and gravity waves in the topside ionosphere may produce plasma density structures with scale sizes small enough to produce small (~11–12 km) path length differences in the ionogram traces.

[88] 2. Electric fields mapping from the *E* region to the *F* region may create a structured *F* region in the direction perpendicular to the magnetic field with scale sizes small enough to produce the observed discrete ionogram traces. Of course, it is also possible that both of the above processes happen simultaneously.

[89] The radar measurements during the experiment reveal numerous gravity waves in the bottomside *F* region ledge with periods between 15 and 90 min. These bottomside waves are observed to propagate toward the northwest with horizontal wavelengths ranging from 176 to 1725 km and phase speeds of 151–592 m/s; they are likely secondary waves generated when primary gravity waves associated with tropical storm Noel dissipate in the thermosphere about 1000 km southeast of the launch site. The waves detected by the radar are directed in opposition to the model tidal winds expected near midnight at midlatitudes but are consistent in magnitude and propagation direction with the short duration wind measurements made simultaneously by the rocket in the topside ionosphere.

[90] The geometry of the neutral winds and electric fields observed by the rocket as it flew through the spread *F* region is consistent with the requirements for the Perkins instability [*Perkins*, 1973], but the growth rates calculated from the in situ data are too small to explain the sudden onset of spread *F* observed. The observed geometry is also not optimized for the *E-F* coupled instability as proposed by *Cosgrove and Tsunoda* [2004]. To resolve the remaining uncertainties associated with the causes of midlatitude spread *F*, a future experiment could be designed to image horizontal plasma density structures in the *E* region on field lines that traverse the *F* region over Wallops Island and compare these observations to simultaneous measurements of spread *F* by the Wallops dynasonde system. Correlation of the E region structures with high-resolution ionograms from the new Wallops dynasonde system could establish a statistical basis for E-*F* region coupling during midlatitude spread *F*.

[91] **Acknowledgments.** This work was supported by NASA grants NNG04WC19G, NNH07AF501, NNG04WC49G, and NNH08CE12C.

[92] Robert Lysak thanks Robert Stening and another reviewer for their assistance in evaluating this paper.

References

Alexander, M. J., J. R. Holton, and D. R. Durran (1995), The gravity wave response above deep convection in a squall line simulation, *J. Atmos. Sci.*, *52*, 2212–2226.

Basu, S., et al. (2005), Two components of ionospheric plasma structuring at midlatitudes observed during the large magnetic storm of October 30, 2003, *Geophys. Res. Lett.*, *32*, L12S06, doi:10.1029/2004GL021669.

Bauer, S. J. (1958), An apparent ionospheric response to the passage of hurricanes, *J. Geophys. Res.*, *63*(1), 265–269, doi:10.1029/JZ063i001p00265.

Behnke, R. (1979), *F* layer height bands in the nocturnal ionosphere over Arecibo, *J. Geophys. Res.*, *84*(A3), 974–978, doi:10.1029/JA084iA03p00974.

Bhaneja, P., G. D. Earle, R. L. Bishop, T. W. Bullett, J. Mabie, and R. Redmon (2009), A statistical study of midlatitude spread *F* at Wallops Island, Virginia, *J. Geophys. Res.*, *114*, A04301, doi:10.1029/2008JA013212.

Bibl, K., and B. W. Reinisch (1978), The universal digital ionosonde, *Radio Sci.*, *13*(3), 519–530, doi:10.1029/RS013i003p00519.

Bishop, R. L., N. Aponte, G. D. Earle, M. Sulzer, M. F. Larsen, and G. S. Peng (2006), Arecibo observations of ionospheric perturbations associated with the passage of Tropical Storm Odette, *J. Geophys. Res.*, *111*, A11320, doi:10.1029/2006JA011668.

Bowman, G. G. (1990), A review of some recent work on midlatitude spread *F* occurrence as detected by ionosondes, *J. Geomag. Geoelectr.*, *42*, 109–138.

Bowman, G. G. (1991), Ionospheric frequency spread and its relationship with range spread in midlatitude regions, *J. Geophys. Res.*, *96*(A6), 9745–9753, doi:10.1029/91JA00389.

Brown, D. P. (2008), *Tropical Cyclone Report: Hurricane Noel*, Natl. Hurricane Center.

Cosgrove, R. B. (2007), Generation of mesoscale *F* layer structure and electric fields by the combined Perkins and Es layer instabilities, in simulations, *Ann. Geophys.*, *25*, 1579.

Cosgrove, R. B., and R. T. Tsunoda (2001), Polarization electric fields sustained by closed-current dynamo structures in midlatitude sporadic *E*, *Geophys. Res. Lett.*, *28*(8), 1455, doi:10.1029/2000GL012178.

Cosgrove, R. B., and R. T. Tsunoda (2002a), Wind-shear-driven, closed-current dynamos in midlatitude sporadic *E*, *Geophys. Res. Lett.*, *29*(2), 1020, doi:10.1029/2001GL013697.

Cosgrove, R. B., and R. T. Tsunoda (2002b), A direction-dependent instability of sporadic *E* layers in the nighttime midlatitude ionosphere, *Geophys. Res. Lett.*, *29*(18), 1864, doi:10.1029/2002GL014669.

Cosgrove, R. B., and R. T. Tsunoda (2004), Instability of the *E-F* coupled nighttime midlatitude ionosphere, *J. Geophys. Res.*, *109*, A04305, doi:10.1029/2003JA010243.

Crowley, G. (1985), Doppler radar studies of the Antarctic ionosphere, Ph. D. thesis, Univ. of Leicester, UK.

Crowley, G., and I. W. McCrea (1988), A synoptic study of TIDs observed in the UK during the first WAGS campaign, October 10–18, 1985, *Radio Sci.*, *23*(6), 905–917, doi:10.1029/RS023i006p00905.

Crowley, G., T. B. Jones, and J. R. Dudeney (1987), Comparison of short period TID morphologies in Antarctica during geomagnetically quiet and active intervals, *J. Atmos. Terr. Phys.*, *49*, 155.

Earle, G. D., A. M. Musumba, and S. L. Vadas (2008), Satellite-based measurements of gravity wave-induced midlatitude plasma density perturbations, *J. Geophys. Res.*, *113*, A03303, doi:10.1029/2007JA012766.

Fahleson, U. V., M. C. Kelley, and F. S. Mozer (1970), Investigation of the operation of a d.c. electric field detector, *Planet. Space Sci.*, *18*, 1551–1561.

Georges, T. M. (1968), HF Doppler studies of TIDs, *J. Atmos. Terr. Phys.*, *30*(5), 735–746.

Haldoupis, C., and K. Schlegel, and D. T. Farley (1996), An explanation for Type 1 radar echoes from the midlatitude E region ionosphere, *Geophys. Res. Lett.*, *23*(1), 97–100, doi:10.1029/95GL03585.

Haldoupis, C., M. C. Kelley, G. C. Hussey, and S. Shalimov (2003), Role of unstable sporadic *E* layers in the generation of midlatitude spread F, *J. Geophys. Res.*, *108*(A12), 1446, doi:10.1029/2003JA009956.

Hanson, W. B., and F. S. Johnson (1992), Lower midlatitude ionospheric disturbances and the Perkins instability, *Planet. Space Sci.*, *40*, 1615–1630.

Hanson, W. B., U. Ponzi, C. Arduini, and M. DeRuscio (1992), A satellite anemometer, *J. Astronaut. Sci.*, *40*(3), 429–438.

Hines, C. O. (1960), Internal atmospheric gravity waves at ionospheric heights, *Can. J. Phys.*, *38*, 1441–1480.

Hocke, K., and K. Schlegel (1996), A review of atmospheric gravity waves and traveling ionospheric disturbances: 1982–1995, *Ann. Geophys.*, *14*, 917–940.

Hooke, W. H. (1968), Ionospheric irregularities produced by internal atmospheric gravity waves, *J. Atmos. Terr. Phys.*, *30*, 795.

Kelley, M. C. (1997), In situ ionospheric observations of severe weather-related gravity waves and associated small-scale plasma structure, *J. Geophys. Res.*, *102*(A1), 329–335, doi:10.1029/96JA03033.

Kelley, M. C., J. J. Makela, W. E. Swartz, S. C. Collins, S. Thonnard, N. Aponte, and C. A. Tepley (2000), Carribean Ionosphere Camapign, Year One: Airglow and plasma observations during two intense midlatitude spread F events, *Geophys. Res. Lett.*, *27*(18), 2825–2828, doi:10.1029/2000GL000022.

Klostermeyer, J. (1972), Numerical calculation of gravity wave propagation in a realistic thermosphere, *J. Atmos. Terr. Phys.*, *34*, 765–774.

Mathews, J. D., and R. M. Harper (1972), Incoherent scatter radar observations of spread F producing ionospheric structures at Arecibo, *J. Atmos. Terr. Phys.*, *34*, 1119–1127.

Miller, C. A. (1997), Electrodynamics of midlatitude spread *F*: 2. A new theory of gravity wave electric fields, *J. Geophys. Res.*, *102*(A6), 11,533–11,538, doi:10.1029/96JA03840.

Oliver, W. L., Y. Otsuka, M. Sato, T. Takami, and S. Fukao (1997), A climatology of *F* region gravity wave propagation over the middle and upper atmosphere, *J. Geophys. Res.*, *102*(A7), 14,499–14,512, doi:10.1029/97JA00491.

Perkins, F. W. (1973), Spread *F* and ionospheric currents, *J. Geophys. Res.*, *78*(1), 218–226, doi:10.1029/JA078i001p00218.

Reinisch, B. W., K. Bibl, D. F. Kitrosser, G. S. Sales, J. S. Tang, Z. Zhang, T. W. Bullett, and J. A. Rallas (1989), The Digisonde 256 Ionospheric Sounder, World Ionosphere/Thermosphere Study, WITS Handbook, vol. 2, edited by C. H. Liu, chap. 13.

Rishbeth, H., and C. J. Davis (2001), The 70th anniversary of ionospheric sounding, *Eng. Sci.*, 139–144.

Rottger, J. (1977), Travelling disturbances in the equatorial ionosphere and their association with penetrative cumulus convection, *J. Atmos. Terr. Phys.*, *39*, 987–998.

Shalimov, S., C. Haldoupis, and K. Schlegel (1998), Large polarization electric fields associated with midlatitude sporadic *E*, *J. Geophys. Res.*, *103*(A6), 11,617–11,625, doi:10.1029/97JA03666.

Tsunoda, R. T., and R. B. Cosgrove (2001), Coupled electrodynamics in the nighttime midlatitude ionsphere, *Geophys. Res. Lett.*, *28*(22), 4171, doi:10.1029/2001GL013245.

Vadas, S. L. (2007), Horizontal and vertical propagation and dissipation of gravity waves in the thermosphere from lower atmospheric and thermospheric sources, *J. Geophys. Res.*, *112*, A06305, doi:10.1029/2006JA011845.

Vadas, S. L., and G. Crowley (2010), Sources of the traveling ionospheric disturbances observed by the ionospheric TIDDBIT sounder near Wallops Island on 30 October 2007, *J. Geophys. Res.*, *115*, A07324, doi:10.1029/2009JA015053.

Vadas, S. L., and H.-L. Liu (2009), The generation of large-scale gravity waves and neutral winds in the thermosphere from the dissipation of convectively generated gravity waves, *J. Geophys. Res.*, *114*, A10310, doi:10.1029/2009JA014108.

Vadas, S. L., J. Yue, C.-Y. She, P. A. Stamus, and A. Liu (2009), A model study of the effects of winds on concentric rings of gravity waves from a convective plume near Fort Collins on 11 May 2004, *J. Geophys. Res.*, *114*, D06103, doi:10.1029/2008JD010753.

Yokoyama, T., D. L. Hysell, Y. Otsuka, and M. Yamamoto (2009), Three-dimensional simulation of the Perkins and E layer instabilities in the nighttime midlatitude ionosphere, *J. Geophys. Res.*, *114*, A03308, doi:10.1029/2008JA013789.

A. Barjatya, Physical Sciences Department, Embry-Riddle Aeronautical University, 600 S. Clyde Morris Blvd., Daytona Beach, FL 32114, USA.

P. Bhaneja, NGDC, CIRES, 325 Broadway E/GC2, Boulder, CO 80305, USA. (preeti.bhaneja@noaa.gov)

R. L. Bishop, The Aerospace Corporation, PO Box 92957, M2/260, Los Angeles, CA 90009-2957, USA.

T. W. Bullett, Space Weather Observations and Applications, NDGC, CIRES, 325 Broadway E/GC2, Boulder, CO 80305, USA.

R. Cosgrove, Center for Geospace Studies, SRI International, 333 Ravenswood Ave., Menlo Park, CA 94025, USA.

G. Crowley, Atmospheric and Space Technology Research Associates LLC, 11118 Quail Pass, San Antonio, TX 78249, USA.

G. D. Earle, William B. Hanson Center for Space Sciences, University of Texas at Dallas, 800 W. Campbell Rd. WT 15, Richardson, TX 75080, USA.

K. Groves and P. A. Roddy, Air Force Research Laboratory, Space Vehicles Directorate, 29 Randolph Rd., Hanscom AFB, MA 01731, USA.

R. Redmon, NOAA, NGDC, 325 Broadway E/GC2, Boulder, CO 80305, USA.

C. M. Swenson, Department of Electrical and Computer Engineering, Utah State University, 4120 Old Main Hill, Logan, UT 84322, USA.

S. L. Vadas, CoRA Division, NorthWest Research Associates, 3380 Mitchell Ln., Boulder, CO 80503, USA.